学位論文

Solid-Fluid Phase Transitions and Critical Phenomena of Hard-Core Systems

（ハードコア系の固相流相転移と臨界現象）

平成7年12月 博士（理学）申請

東京大学大学院 理学系研究科 物理学専攻

服 金 喜 昭

①

Thesis

Solid–Fluid Phase Transitions and Critical Phenomena of Hard-Core Systems

Synge Todo

Department of Physics, University of Tokyo

Acknowledgments

I would like to express my gratitude to Prof. Masuo Suzuki for his helpful discussions, critical reading of the manuscript, and continual encouragement.

I would like to thank Prof. B. J. Alder for his encouraging comment. I am grateful to Dr. N. Kawashima, Dr. N. Ito and all the members of Suzuki group for useful comments and stimulating discussions.

I am also thankful to Dr. N. Hatano and Dr. Y. Nonomura for their critical reading of the manuscript.

Numerical calculations in the present thesis were performed on the HITAC S-3800/480 in the Computer Center of the University of Tokyo and on the HP Appolo 9000/735 and 710 at Suzuki laboratory in the University of Tokyo.

Finally, I thank my family for their continual encouragement.

Contents

List of Figures

List of Tables

CHAPTER 1

General Introduction

The existence of matter in three different phases (namely, solid, liquid, and gas phases) is experienced everyday. Under ordinary circumstances, a transition between three phases is of first order rather than of continuous one. The first-order transition is associated with latent heat. When a liquid makes a first-order transition into a solid, a non-zero quantity of heat, namely the latent heat, is emitted outside as the liquid cools through an infinitesimally small temperature range around the transition temperature. This emission of heat at the transition tells us that the structure of fluid is being reordered at the transition point.

The gas–liquid phase transition line terminates in a point (FIGURE 1.1). This point is referred to as the *critical point*. At the critical point the phase transition becomes continuous and it is believed to belong to the same universality class as the Ising model. The fact that the gas–liquid transition line does not extend forever enables us to convert a gas to a liquid continuously without crossing the transition line, which was first pointed out explicitly by van der Waals. In this sense there is no fundamental difference between the gas and liquid (thus, we prefer to call *fluid* rather than *gas* or *liquid* above the critical temperature).

On the other hand, the solid–fluid coexistence line has no critical point and extends forever, because the solid and fluid phases have different symmetries with each other. The fluid phase has a fully translational symmetry, while the solid phase has only a discrete one. *A given symmetry element is whether there is or not; there is no way for it to grow imperceptibly* [1]. Then, one can always discriminate with the solid and fluid phases.

Hard-core model and its athermal property. In general, the interacting potential of a simple gas consists of two portions; short-ranged-repulsive and long-ranged-attractive parts (FIGURE 1.2). The attractive portion has some finite depth, while the repulsive portion of the potential extends upward without limit. At high temperatures, the attractive part of the reduced potential becomes negligible compared with the infinite repulsive part. So the hard-core model seems intuitively reasonable as a high-temperature limit of a gas.

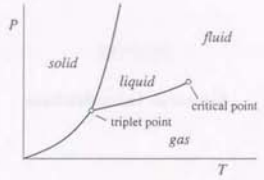

FIGURE 1.1. Phase diagram of a simple fluid.

In addition, it is experimentally observed that at high temperatures the solid–fluid coexistence curve tends towards a *straight line* in the pressure–temperature phase diagram. That is, the reduced pressure P/kT is deprived of the temperature dependence. This experimental observation gives another justification for the hard-core potential as a theoretical model describing solid–fluid phase transitions, at least, at high temperatures. In the case of the hard-core potential, the energy of the system is all kinetic, with no volume dependence (assuming that classical mechanics applies). Therefore, the second term on *l.h.s.* of the following thermodynamic equation of state:

$$P = T\left(\frac{\partial S}{\partial V}\right)_{T,N} - \left(\frac{\partial E}{\partial V}\right)_{T,N} \tag{1.1}$$

must vanish. By using Maxwell's relationship:

$$\left(\frac{\partial S}{\partial V}\right)_{T,N} = \left(\frac{\partial P}{\partial T}\right)_{V,N}, \tag{1.2}$$

we obtain, at constant V and N,

$$\frac{dP}{P} = \frac{dT}{T}, \tag{1.3}$$

which is easily integrated to give

$$\frac{P}{kT} = \Gamma(\rho). \tag{1.4}$$

Here the function $\Gamma(\rho)$, which does not depend on the temperature, contains all thermodynamic information of the hard-core system [2]. Thus, the transition line of the hard-core system appears as a straight line in its pressure–temperature phase diagram. There is only one independent intensive variable, which is usually taken to be the density ρ or the reduced chemical potential μ/kT in the canonical and grand-canonical formalisms, respectively.

Lattice-gas model. The 'lattice gas' was introduced in the late thirties as a mathematically simplified model of an ordinary continuous fluid [3,4]. In the lattice-gas model, the center-of-mass of molecules is restricted on the vertices of some regular array or lattice. Since every lattice site is occupied by a molecule or vacant, there is

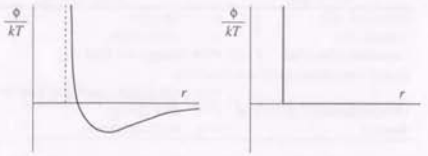

FIGURE 1.2. Reduced interacting potential ϕ/kT between two particles in a distance of r (left) and its high-temperature limit (right).

a natural description of a binary nature for every configuration. The similarity with a magnetic system of spin 1/2 provides a convenient starting point for the presentation of the lattice gas.

Indeed, there is a one-to-one correspondence between the thermodynamic variables of the lattice gas and the magnetic variables of spin systems [5]. Especially, as was proven by Yang and Lee [6], there is a mathematical equivalence between the *Ising* model and the lattice gas (TABLE 1.1). In terms of this equivalence, the hard-core lattice gas can be interpreted as a special limit, namely, a low-temperature limit, of an antiferromagnetic Ising model in a non-vanishing field.

In 1962, Alder and Wainwright demonstrated the existence of a first-order phase transition, the Alder transition, of hard disks on continuous space, by means of the molecular-dynamics method [7]. On the contrary, as is well known, the nearest-neighbor Ising antiferromagnet, which is the simplest non-trivial model describing the solid–fluid phase transition, exhibits a phase transition of second order. An interesting question is the way in which a lattice gas approaches the continuum limit.

Another attitude to the lattice-gas models is possible. An adsorbed monolayer on substrates, such as H on Pd or Kr on graphite, can be considered as an example of physical realizations of the lattice-gas model. It is experimentally observed that these monolayers have various structures, and exhibit various non-trivial phase transitions. In the theoretical approach, on the other hand, order–disorder transitions of second order on two-dimensional lattices are indicated to be classified into a small number of universality classes in terms of a criterion by Landau [8,9].

Transfer-matrix method. The transfer-matrix method was introduced by Kramers and Wannier [10,11], and has been applied with great success in the study of statistical mechanical models for finding exact solutions in one and two dimensions [12,13]. On the other hand, this method has also been used extensively in numerical investigations [14]. In comparison with the Monte Carlo simulation, the transfer-matrix method has some advantages: It is free not only from statistical errors, but also from the difficulty of *critical slowing down*, which prevents the Monte Carlo results from converging rapidly.

Moreover, in two dimensions, the *conformal invariance* associated with a critical system yields a great deal of beautiful consequences [15–18]. This is due to the fact

lattice gas		Ising model
occupied site	$\longleftrightarrow$	up spin
vacant site	$\longleftrightarrow$	down spin
chemical potential	$\longleftrightarrow$	magnetic field
grand canonical partition function	$\longleftrightarrow$	canonical partition function
thermodynamic potential	$\longleftrightarrow$	free energy
density	$\longleftrightarrow$	magnetization

TABLE 1.1. Correspondence between the lattice gas and the Ising model.

that the group of conformal transformations in two dimensions has an infinite dimensionality. Combined with the finite-size scaling [19–27] and the conformal invariance, the transfer-matrix method becomes one of the most powerful numerical methods in investigating two-dimensional classical, or almost equivalently one-dimensional quantum systems.

In general, exact calculations in terms of transfer matrices require much memory storage, which increases exponentially as the system size increases, while the Monte Carlo simulations have a limitation coming mainly from the computational time. Currently, the dimension of the transfer matrix can not exceed a few times of 10^7, which means that the maximum system size tractable on current super computers is about 24 for a nearest-neighbor Ising model.

However, in some special cases such as hard-core models, the dimension of the transfer matrix can be highly reduced owing to the presence of infinite repulsions or other restrictions on configuration space. Combined with the sparse-matrix-factorization scheme, which is a standard technique in computations on large-scale matrices, it makes possible to perform exact calculations of the transfer matrices efficiently for much larger systems than before.

It should be emphasized that in a usual manner the above dimensional reduction is *not compatible* with the matrix factorization into sparse ones. It needs some additional techniques for them to get along together.

Overviews of the succeeding chapters. In the present thesis, we discuss solid–fluid phase transitions in systems with hard-core potential. In chapters 2 and 3, we apply the transfer-matrix method with the dimensional reduction and sparse-matrix factorization to the two-dimensional classical and one-dimensional quantum lattice-gas models with hard-core potential, respectively. In chapter 2, we also discuss interacting hard-core lattice gases on the triangular and square lattices and find their phase diagrams. In chapter 4, we investigate the continuum hard-core models, which is expected to exhibit a first-order transition, by means of the virial series expansion and the coherent-anomaly method. In appendices, we discuss in detail our new method to treat large-scale transfer matrices of the hard-core lattice gases.

CHAPTER 2

Classical Lattice Gas in Two Dimensions

2.1. Introduction

In the present chapter we consider two-dimensional hard-core lattice gases with next-nearest-neighbor interaction on the triangular and square lattices. The reduced Hamiltonian of our models is generally defined as follows:

$$-\beta\mathcal{H} = U\sum_i n_i + W_1\sum_{\langle i,j\rangle_1} n_i n_j + W_2\sum_{\langle i,j\rangle_2} n_i n_j\,, \tag{2.1}$$

where $U = \beta\mu$ is the reduced chemical potential, $W_1 = -\beta w_1 = -\infty$ the infinite repulsion between nearest-neighbor sites, $W_2 = -\beta w_2$ the reduced next-nearest-neighbor interaction (attractive for $W_2 > 0$ and repulsive for $W_2 < 0$), and $n_i = 1$ or 0 denotes whether the ith site is occupied or vacant. The subscript $\langle i,j\rangle_k$ denotes that the summation should be taken over all kth-nearest-neighbor pairs.

The lattice-gas Hamiltonian (2.1) is shown to be mathematically equivalent to the Ising model with non-vanishing magnetic field [6]. By introducing Ising variables $s_i = 2n_i - 1 = \pm 1$, the Hamiltonian (2.1) can be rewritten into the following Ising Hamiltonian:

$$-\beta\mathcal{H}^{(I)} = E_0 + h\sum_i s_i + K_1\sum_{\langle i,j\rangle_1} s_i s_j + K_2\sum_{\langle i,j\rangle_2} s_i s_j\,, \tag{2.2}$$

where K_1 is the reduced nearest-neighbor interaction, K_2 the reduced next-nearest-neighbor interaction, h the reduced magnetic field, and E_0 is a trivial background energy shift. They are expressed in terms of W_1, W_2, and U as

$$\begin{aligned} E_0 &= (U + z_1W_1 + z_2W_2)\,V/2 \\ K_1 &= W_1/4 \\ K_2 &= W_2/4 \\ h &= (2U + z_1W_1 + z_2W_2)/4\,, \end{aligned} \tag{2.3}$$

where V is the volume of the system (the number of the lattice sites) and z_i is the number of the ith-nearest neighbors of a lattice site (z_1 is usually referred to as the *coordination number*. $z_1 = z_2 = 6$ for the triangular lattice and $z_1 = z_2 = 4$ for

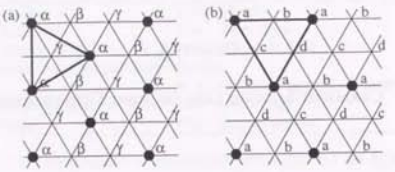

FIGURE 2.1. Ground-state configurations on the triangular lattice. (a) $\sqrt{3}\times\sqrt{3}$ structure and the three equivalent interpenetrating sublattices (α, β, and γ). (b) 2×2 structure and the four equivalent sublattices (a, b, c, and d).

the square lattice). Thus, the attractive (repulsive) interaction between two particles corresponds to the ferromagnetic (antiferromagnetic) interaction between two spins. The grand canonical partition function of the lattice gas is also equivalent to the canonical partition function of the Ising model (see TABLE 1.1 on p. 4).

The hard-core limit $W_1 \to -\infty$ in Eq. (2.1) is equivalent to a low-temperature limit $K_1 \to -\infty$ of the Ising Hamiltonian (2.2) with K_2 and $(h - z_1K_1 - z_2K_2)$ fixed. Therefore, a critical point of the hard-core lattice gas corresponds to the *slope* of the critical line in the temperature–field phase diagram of the Ising model in the low-temperature limit.

In the present chapter we investigate the phase diagrams and the universality classes of the phase transitions of the two-dimensional hard-core lattice gases in terms of transfer-matrix method with the finite-size scaling [19–21, 26, 27] and the conformal invariance [15–18]. By applying the dimensional reduction and the sparse-matrix factorization, we perform exact diagonalization for much larger systems than the previous works.

2.2. Ground States and Order Parameters

In the disordered phase, all the symmetries associated with the Hamiltonian (2.1) are conserved. At a transition point some of such symmetries would break spontaneously. To speculate which symmetries break and what long-range orders appear in ordered phases, in the present section we first review ground-state symmetries, realized ordered phases, and their order parameters.

2.2.1. Triangular lattice. On the triangular lattice, three different configurations can be realized in the low-temperature limit; $\sqrt{3}\times\sqrt{3}$, 2×2, and the *completely vacant state* (hereafter, simply referred to as '*empty state*'), which are shown in FIGURE 2.1.

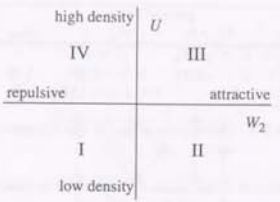

FIGURE 2.2. Four regions in the parameter space (W_2, U).

The energy *per site* in each configuration is respectively given by

$$\beta E = \begin{cases} -U/3 - W_2 & \text{for } \sqrt{3}\times\sqrt{3} \\ -U/4 & \text{for } 2\times 2 \\ 0 & \text{for empty state.} \end{cases} \tag{2.4}$$

Now we divide the parameter space (W_2, U) into four regions (FIGURE 2.2):

Region I : $W_2 < 0$ and $U < 0$
II : $W_2 > 0$ and $U < 0$
III : $W_2 > 0$ and $U > 0$
IV : $W_2 < 0$ and $U > 0$

In the region I, the second-nearest-neighbor interaction W_2 is repulsive, and negative U prefers low densities. Clearly, the ground state is the empty state. In the region III, the ground state is specified by $\sqrt{3}\times\sqrt{3}$, the most dense configuration. On the other hand, in the region II, negative U and attractive W_2 compete with each other. A phase boundary in the ground state is determined by comparing the ground-state energy (2.4) between the $\sqrt{3}\times\sqrt{3}$ state and the empty state, and consequently we obtain $U = -3W_2$. Finally, in the region IV, the competing positive U and repulsive W_2 cause a ground-state phase transition between the $\sqrt{3}\times\sqrt{3}$ and 2×2 states at $U = -12W_2$.

At the $\sqrt{3}\times\sqrt{3}$ ground state, one of the three equivalent interpenetrating sublattices (α, β, and γ in FIGURE 2.1 (a)) is fully occupied and the others are completely vacant. That is, the three-sublattice symmetry breaks down in this phase. We introduce the sublattice densities:

$$\rho_k = \frac{3}{N}\sum_{i\in k} n_i \qquad (k = \alpha, \beta, \gamma)\,. \tag{2.5}$$

In terms of these sublattice densities, we define an order parameter, which consists of three components, of the $\sqrt{3}\times\sqrt{3}$ phase:

$$\phi_k = \rho_k - \rho \qquad (k = \alpha, \beta, \gamma)\,, \tag{2.6}$$

	ground state				
order	$W_2 > 0$	$W_2 < 0$	ρ_{max}	ϕ	θ
disordered	$U < -3W_2$	$U < 0$	—	0	0
$\sqrt{3} \times \sqrt{3}$	$U > -3W_2$	$U > -12W_2$	1/3	$\neq 0$	0
2×2	—	$0 < U < -12W_2$	1/4	0	$\neq 0$

TABLE 2.1. Order parameters on the triangular lattice.

and the corresponding root-mean-squares (RMS) order parameter:

$$\begin{aligned} \phi_{\text{RMS}} &= \sqrt{\phi_\alpha^2 + \phi_\beta^2 + \phi_\gamma^2} \\ &= \sqrt{\rho_\alpha^2 + \rho_\beta^2 + \rho_\gamma^2 - 3\rho^2}\,, \end{aligned} \tag{2.7}$$

where we have used the relation, $\rho = \frac{1}{3}(\rho_\alpha + \rho_\beta + \rho_\gamma)$.

In the 2×2 phase, on the other hand, another symmetry, that is, the four-sublattice symmetry, is broken. In this case, we divide the triangular lattice into the *four* equivalent sublattices, as shown in FIGURE 2.1 (b), and define the corresponding sublattice densities:

$$\rho_k = \frac{4}{N} \sum_{i \in k} n_i \qquad (k = \text{a,b,c,d})\,. \tag{2.8}$$

By using these sublattice densities, we define a four-component order parameter of the 2×2 phase:

$$\theta_k = \rho_k - \rho \qquad (k = \text{a,b,c,d})\,, \tag{2.9}$$

and the corresponding RMS order parameter:

$$\begin{aligned} \theta_{\text{RMS}} &= \sqrt{\theta_{\text{a}}^2 + \theta_{\text{b}}^2 + \theta_{\text{c}}^2 + \theta_{\text{d}}^2} \\ &= \sqrt{\rho_{\text{a}}^2 + \rho_{\text{b}}^2 + \rho_{\text{c}}^2 + \rho_{\text{d}}^2 - 4\rho^2}\,. \end{aligned} \tag{2.10}$$

We summarize the ordered phases on the triangular lattice and their order parameters in TABLE 2.1.

2.2.2. Square lattice. In the case of the square lattice, the ground-state phase diagram is topologically the same as on the triangular lattice, but the structures appearing therein are quit different. On the square lattice, three different structures, $\sqrt{2} \times \sqrt{2}$, 2×1, and a trivial *empty state*, appear in the ground state, which have the following energy density:

$$\beta E = \begin{cases} -U/2 - W_2 & \text{for } \sqrt{2} \times \sqrt{2} \\ -U/4 & \text{for } 2 \times 1 \\ 0 & \text{for empty state.} \end{cases} \tag{2.11}$$

The empty state and the $\sqrt{2} \times \sqrt{2}$ state appear in the regions I and III, respectively. In the region II, the phase boundary between the empty state and the $\sqrt{2} \times \sqrt{2}$ state is given by $U = -2W_2$.

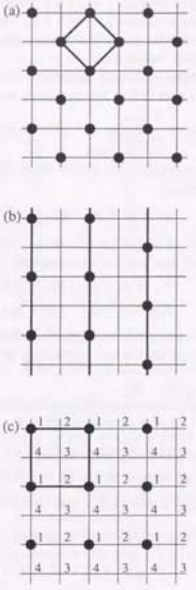

FIGURE 2.3. Ground-state configurations on the square lattice. (a) $\sqrt{2} \times \sqrt{2}$ structure. (b) 2×1 structure. Every other row, denoted by thick lines, is ordered antiferromagnetically in the vertical direction. However, they are *not* ordered with respect to each other. (c) 2×2 structure and the four equivalent interpenetrating sublattices (1, 2, 3, and 4).

In the region IV, the $\sqrt{2}\times\sqrt{2}$ state is stable for $U > -4W_2$. On the contrary, a highly degenerate structure appears for $0 < U < -4W_2$, where antiferromagnetic-like rows alternate with empty rows. The antiferromagnetic rows, in which every other site is occupied, are *not* ordered with respect to each other (FIGURE 2.3 (b)). Therefore, the ground state degeneracy is given by $4 \times 2^{\sqrt{V}/2}$, where V is the volume of the system. Although the residual entropy ($\sim \sqrt{V}$) is infinite in the thermodynamic limit, it is not extensive. This state is referred to as 2×1. The occupied sites exhibit a long-range order only in one direction, while the vacant sites have a true two-dimensional long-range order as mentioned below.

We divide the square lattice into four equivalent interpenetrating sublattices (1, 2, 3, and 4 in FIGURE 2.3 (c)) and define the densities on each sublattice:

$$\rho_k = \frac{4}{N}\sum_{i\in k} n_i \qquad (k = 1,2,3,4)\,. \tag{2.12}$$

In terms of the sublattice densities, we define three kinds of order parameters. The first one is the *staggered* density:

$$\rho_s = \rho_1 + \rho_3 - (\rho_2 + \rho_4)\,, \tag{2.13}$$

which is an order parameter of the $\sqrt{2}\times\sqrt{2}$ phase. On the other hand, it vanishes in the 2×1 phase. The second one has two components and is defined as

$$\begin{aligned}\theta_{12} &= \rho_1 + \rho_2 - (\rho_3 + \rho_4)\\ \theta_{23} &= \rho_2 + \rho_3 - (\rho_4 + \rho_1)\,,\end{aligned} \tag{2.14}$$

which corresponds to the *superantiferromagnetic* order parameter in the language of spin systems. One may introduce the corresponding RMS order parameter:

$$\begin{aligned}\theta_{\text{RMS}} &= \sqrt{\theta_{12}^2 + \theta_{34}^2}\\ &= \sqrt{2(\rho_1^2 + \rho_2^2 + \rho_3^2 + \rho_4^2) - 4(\rho_1\rho_3 + \rho_2\rho_4)}\,.\end{aligned} \tag{2.15}$$

The last one has four components, which is defined as

$$\phi_k = \rho_k - \rho \qquad (k = 1,2,3,4). \tag{2.16}$$

The corresponding RMS order parameter is also defined as

$$\begin{aligned}\phi_{\text{RMS}} &= \sqrt{\phi_1^2 + \phi_2^2 + \phi_3^2 + \phi_4^2}\\ &= \sqrt{\rho_1^2 + \rho_2^2 + \rho_3^2 + \rho_4^2 - 4\rho^2}\,.\end{aligned} \tag{2.17}$$

In the $\sqrt{2}\times\sqrt{2}$ phase, the two-sublattice symmetry breaks spontaneously, e.g., $\rho_s \neq 0$. On the other hand, in the 2×1 phase, the staggered density ρ_s vanishes, but both θ and ϕ remain finite, that is, the four-sublattice symmetry breaks in this phase, but that of two sublattices does *not*. If we introduce third-nearest-neighbor attraction, it would be expected that the highly degenerated 2×1 structure is *frozen* into the 2×2 state, where the ground state has only four-fold degeneracy (FIGURE 2.3). In the 2×2 phase, all the order parameters defined above have finite values. Thus, by means of ρ_s, θ, and ϕ, one can discriminate between the $\sqrt{2}\times\sqrt{2}$, 2×1, and 2×2 phases (TABLE 2.2).

	ground state					
order	$W_2 > 0$	$W_2 < 0$	$\rho_{\max}$	ρ_s	θ	ϕ
disordered	$U < -2W_2$	$U < 0$	—	0	0	0
$\sqrt{2}\times\sqrt{2}$	$U > -2W_2$	$U > -4W_2$	1/2	$\neq 0$	0	$\neq 0$
2×1	—	$0 < U < -4W_2$	1/4	0	$\neq 0$	$\neq 0$
2×2	—	—	1/4	$\neq 0$	$\neq 0$	$\neq 0$

TABLE 2.2. Order parameters on the square lattice. The 2×2 order does not appear in the next-nearest-neighbor model. It is expected to appear in the presence of the third-nearest-neighbor attraction.

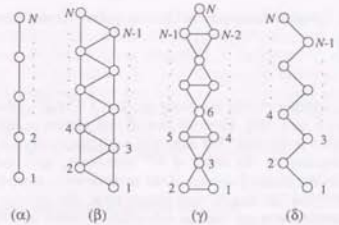

FIGURE 2.4. Unit slices of the transfer matrices.

2.3. Transfer-Matrix Method and Phenomenological Renormalization

Consider a lattice of infinite length in one direction (referred to as the *transfer* direction). In the other direction (the *length* direction), the periodic boundary conditions are applied. A first step to introduce a transfer matrix is to divide the lattice sites into a one-dimensional array of *unit slices*. These unit slices have to satisfy the following conditions:

(i) All the unit slices should be geometrically identical.
(ii) The total Hamiltonian can be written as a *sum* of neighboring-two-slice Hamiltonians.

The second condition can be put in another way:

(ii') If one removes a unit slice from the lattice, the remaining sites should be separated into the two portions which do not interact with each other.

The last condition persists that in the case of a model with second-nearest-neighbor interaction, the unit slice is not a simple linear chain any more. It should be taken as a double chain or other complicated forms (FIGURE 2.4). As a consequence, the dimension of the transfer matrix of the next-nearest-neighbor model becomes quite large, compared with the model only with the nearest-neighbor interaction. This fact makes it hard to perform numerical diagonalization for large systems.

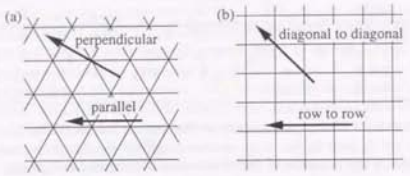

FIGURE 2.5. Transfer directions on the triangular (a) and square (b) lattices.

In general, the transfer matrix is a dense matrix of $2^N \times 2^N$, where N is the number of sites included in a unit slice. However, use of this matrix in this form in numerical applications is highly inefficient. For example, multiplication of a trial vector by the transfer matrix requires on the order of 2^{2N} elementary arithmetic operations. In addition, it requires the memory storage of the same order to store the matrix elements. However, by factorizing the matrix into sparse ones, the number of operations and the use of the memory storage can be extremely reduced as $O(N2^N)$ and $O(2^N)$, respectively [14].

On the other hand, if there is infinite repulsion, a quite number of elements of the transfer matrix should vanish. Especially, the number of rows or columns which have at least one non-vanishing element is roughly λ^N ($\ll 2^N$), where $1 < \lambda < 2$ (see appendix B). Thus, the transfer matrix becomes effectively a $\lambda^N \times \lambda^N$ matrix rather than $2^N \times 2^N$. The number of operations and the use of the memory storage therefore can be reduced as $O(\lambda^{2N})$. However, in general, this dimensional reduction and the sparse-matrix factorization above mentioned are not compatible at all with each other. It needs some additional technique for them to get along together, which is discussed in detail in appendix A. Our new method can be also applied to the models with next-nearest-neighbor interaction and makes it possible to calculate much larger systems than the previous works.

In the succeeding sections, we use eight types of transfer matrices, which are defined on the different lattices, for different transfer directions (FIGURE 2.5), and for different interactions. We summarize our transfer matrices in TABLE 2.3. Explicit expressions for their sparse-matrix factorization with dimensional reduction are presented in appendix C. Note that the '*size*' N, used hereafter, denotes not the actual physical length (circumference) but the number of sites involved in a unit slice. The actual length L (in unit of the lattice constant) is given by

$$L = \eta N\,, \tag{2.18}$$

type	lattice	direction	interaction	unit slice	configuration space	symmetry	ζ
(a)	triangular	PD	(2+0)	(α)	$\psi_2^{(\alpha)}$	S	$\sqrt{3}$
(b)	square	RR	(2+0)	(α)	$\psi_2^{(\alpha)}$	S	1
(c)	triangular	PD	(2+1)	(β)	$\psi_2^{(\beta)}$	NS	$2\sqrt{3}$
(d)	triangular	PL	(2+1)	(γ)	ϕ	NS	$4\sqrt{3}$
(e)	square	RR	(2+1)	(α)	$\psi_2^{(\alpha)}$	S	1
(f)	square	DD	(2+1)	(δ)	$\psi_2^{(\beta)}$	NS	2
(g)	triangular	PD	(3+0)	(β)	$\psi_3^{(\alpha)}$	NS	$2\sqrt{3}$
(h)	square	DD	(3+0)	(δ)	$\psi_3^{(\alpha)}$	NS	2

TABLE 2.3. Transfer matrices used in the present chapter. In this table we use the following abbreviations: PD (perpendicular), PL (parallel), RR (row to row), DD (diagonal to diagonal), S (symmetric), and NS (non-symmetric). The interaction '$(m+n)$' denotes the exclusion up to $(m-1)$th-nearest neighbor sites and $(m+n-1)$th-nearest-neighbor finite interaction (attractive or repulsive), and '$(m+0)$' denotes to a pure hard-core system. The unit slices $(\alpha), \ldots, (\delta)$ are shown in FIGURE 2.4. For details of the 'configuration space,' see appendix B.

where η is a constant associated with each unit slice:

$$\eta^{-1} = \begin{cases} 1 & \text{for } (\alpha) \\ 2 & \text{for } (\beta) \\ \sqrt{3} & \text{for } (\gamma) \\ \sqrt{2} & \text{for } (\delta)\,. \end{cases} \tag{2.19}$$

For symmetric matrices, as is well known, the (symmetric) *Lanczos method* [28–30] is one of the most powerful methods to calculate eigenvalues. This method has the advantage of yielding several leading eigenvalues simultaneously; the corresponding eigenvectors also can be obtained, but in general they are not so accurate. Another efficient method for symmetric matrices is the *conjugate-gradient method* [29,30]. This method can produce only one eigenvalue at a time together with the corresponding eigenvector. Of course, it is possible to obtain subdominant eigenvalues by using orthogonalization techniques.

For the further-nearest-neighbor models, on the other hand, the transfer matrix generally becomes non-symmetric owing to the geometrical asymmetry in the unit slice. In this case, the (unsymmetric) Lanczos method also works, however, it becomes quite unstable. So we use the simple *power method* [29, 30] to calculate dominant eigenvalues and eigenvectors of non-symmetric matrices. For non-symmetric matrices, one must distinguish the *right* and *left* eigenvectors which are associated with the same eigenvalue, while they are identical in the symmetric case. To obtain a subdominant *right* eigenvector, a trial vector should be orthogonalized with the dominant *left* eigenvectors.

It should be noted that a *left* eigenvector of a matrix $\mathbf{T}$ is a *right* eigenvector of $\mathbf{T}^\dagger$. In general, there exists a matrix $\mathbf{G}$, which satisfies

$$\mathbf{G}^{-1}\cdot\mathbf{T}^\dagger\cdot\mathbf{G}=\mathbf{T} \tag{2.20}$$

for a matrix $\mathbf{T}$. If $\mathbf{v}$ is a *right* eigenvector associated with an eigenvalue λ of a matrix $\mathbf{T}$, then $(\mathbf{G}\cdot\mathbf{v})$ becomes the *left* eigenvector with the eigenvalue λ of $\mathbf{T}$ (or equivalently, a *right* eigenvector of $\mathbf{T}^\dagger$). In fact,

$$\begin{aligned}\mathbf{T}^\dagger\cdot(\mathbf{G}\cdot\mathbf{v})&=(\mathbf{T}^\dagger\cdot\mathbf{G})\cdot\mathbf{v}\\&=(\mathbf{G}\cdot\mathbf{T})\cdot\mathbf{v}\\&=\mathbf{G}\cdot(\mathbf{T}\cdot\mathbf{v})\\&=\mathbf{G}\cdot(\lambda\mathbf{v})\\&=\lambda\,(\mathbf{G}\cdot\mathbf{v})\,.\end{aligned} \tag{2.21}$$

We call the matrix $\mathbf{G}$ as the *conjugation matrix*. For symmetric matrices, one can choose $\mathbf{G}$ as an identity matrix, apparently. On the other hand, for non-symmetric matrices, in general, $\mathbf{G}$ becomes rather complicated. However, in the case of our transfer matrices, it is found to become a simple matrix, which generates a permutation of the lattice sites, owing to the special symmetries associated with the geometrical relation between the unit slices (see appendix C).

Thus, if one calculates a *right* eigenvector, the corresponding *left* eigenvector is also obtained automatically. This property is very useful to calculate subdominant eigenvectors, which need to be orthogonalized with the dominant *conjugate* eigenvector. Moreover, if $\mathbf{v}$ is equal to a right eigenvector up to a contribution of order ϵ, the *modified* Reileigh quotient [31]:

$$\begin{aligned}R(\mathbf{v},\mathbf{w})&=\frac{\mathbf{w}^\dagger\cdot\mathbf{T}\cdot\mathbf{v}}{\mathbf{w}^\dagger\cdot\mathbf{v}}\\&=\frac{(\mathbf{G}\cdot\mathbf{v})^\dagger\cdot\mathbf{T}\cdot\mathbf{v}}{(\mathbf{G}\cdot\mathbf{v})^\dagger\cdot\mathbf{v}}\end{aligned} \tag{2.22}$$

is equal to the corresponding eigenvalue up to a contribution on order ϵ^2, which greatly accelerates the rate of convergence.

Once dominant eigenvalues have been calculated, the reduced pressure P/kT and reduced free-energy density f can be obtained from the largest eigenvalue λ_0 as

$$\frac{P}{kT}=-f=\frac{1}{N}\log\lambda_0\,. \tag{2.23}$$

The density and the compressibility are also given by

$$\rho=-\frac{\partial f}{\partial U}\,, \tag{2.24}$$

$$\chi=\frac{\partial\rho}{\partial U}=-\frac{\partial^2 f}{\partial U^2}\,, \tag{2.25}$$

respectively. In addition, we define the free-energy-density levels $\{f_i\}$:

$$f_i=-\frac{1}{N}\log|\lambda_i|\quad(i=0,1,2,\cdots)\,, \tag{2.26}$$

where λ_i is the $(i+1)$th-largest eigenvalue in absolute magnitude ($f_0=f$).

In terms of the free-energy-density levels, the correlation length, or the *gap*, is given by

$$\xi_{i,N}^{-1}=N(f_i-f_0)\,. \tag{2.27}$$

According to the finite-size scaling [19–21,26,27] and conformal invariance [15–18], the *scaled gap* $N\xi_{i,N}^{-1}$ tends towards a constant at the critical point and, moreover, it has a *universal* value:

$$\frac{N}{\xi_{i,N}(U_c)}=2\pi\zeta x_i\,, \tag{2.28}$$

for $N\to\infty$, where x_n is a scaling dimension of the corresponding correlation function. The constant ζ is called the *geometrical factor* [32], which must be introduced owing to the anisotropy of the scaling field $1/N$. It is given as the ratio of the actual *physical* width of a unit slice of N sites in the transfer direction and the actual *physical* length of a geometrically isotropic lattice. The geometrical factor for our transfer matrices is also listed in TABLE 2.3.

Accordingly, an approximate critical point is obtained as a fixed point of the phenomenological renormalization mapping [22–25]:

$$\frac{N}{\xi_N(U_N^*)}=\frac{N'}{\xi_{N'}(U_N^*)} \tag{2.29}$$

of the leading correlation length $\xi_N\,(=\xi_{1,N})$ for different system sizes, N and N'. One can also use Eq. (2.28) directly with an explicit value of x_i. Note that the approximate critical point by means of Eq. (2.28) converges to the true one, even if an incorrect value is assigned to x_i, but this will cause a much slower convergence than Eq. (2.29).

The thermal exponent y_t can be calculated, using the scaling law:

$$\left.\frac{d(N\xi_N^{-1}(U))}{dU}\right|_{U=U_c}\simeq aN^{y_t}\,. \tag{2.30}$$

In practice, we consider an *effective* thermal exponent $y_{t,N}$, obtained by

$$y_{t,N}=\left\{\log\left(\frac{d(N'\xi_{N'}^{-1}(U))}{dU}\Big/\frac{d(N\xi_N^{-1}(U))}{dU}\right)_{U=U_N^*}\right\}\Big/\log(N'/N)\,. \tag{2.31}$$

The free-energy density at the critical point also has a universal finite-size correction:

$$f(N)|_{U=U_c}=f_\infty-\frac{\pi\zeta c}{6N^2}+\cdots \tag{2.32}$$

for periodic boundary conditions, where c is the central charge of the Virasoro algebra and f_∞ is the reduced free-energy density of the bulk. One can also use the *effective* central charge:

$$c_N=\left.\frac{6N^2N'^2(f(N')-f(N))}{\pi\zeta(N'^2-N^2)}\right|_{U=U_N^*} \tag{2.33}$$

for finite-size analyses.

2.4. Non-Interacting Hard Hexagons and Squares

First we consider the non-interacting case ($W_2 = 0$) for the check of correctness and efficiency of our method. The non-interacting hard-core lattice gas on the triangular lattice (hard hexagons) has been solved exactly by Baxter [33]; a second-order transition to the $\sqrt{3} \times \sqrt{3}$ phase occurs at

$$U_c = \log \frac{11 + 5\sqrt{5}}{2} = 2.406059125\cdots , \tag{2.34}$$

and it belongs to the same universality class as the three-state Potts model ($c = 4/5$). On the contrary, the non-interacting model on the square lattice (hard squares) can not be solved exactly. In connection with the phase diagram of the antiferromagnetic Ising model, this model has been studied extensively by many authors; series expansions [34,35], mean-field approximations and their generalizations [36–39], Monte Carlo simulations [40, 41], transfer-matrix methods *without* the finite-size scaling [42, 43], transfer matrices with the phenomenological renormalization and conformal invariance [44, 45], *etc.*

Especially, Müller-Hartmann and Zittarz [46] derived an analytic expression for the critical line of the Ising antiferromagnet by considering the interfacial tension. Although their method is approximate, it gives the exact critical temperature for zero magnetic field. Unfortunately it is not exact for non-vanishing fields*. Even so, it is a remarkably simple and reasonably accurate approximation.

The best estimate for the critical point of hard squares is obtained by Blöte and Wu [44]:

$$U_c = 1.3340151004(8) , \tag{2.35}$$

by means of the phenomenological renormalization and the conformal invariance. The universality class of the transition is believed to be the same as the Ising ferromagnet ($c = 1/2$), and has been numerically confirmed very accurately [45].

The transfer matrices for hard hexagons and squares (type (a) and (b) in TABLE 2.3) are calculated for $N = 3, 6, 9, \cdots, 27$ and $2, 4, 6, \cdots, 28$, respectively. To obtain an approximate critical point, we use Eq. (2.28) instead of Eq. (2.29), because the former is slightly more robust to rounding errors in computer calculations. The leading scaling dimension x_σ, which corresponds to the order–order correlation function, is given by

$$x_\sigma = \begin{cases} 2/15 & \text{for the three-state Potts universality class,} \\ 1/8 & \text{for the Ising universality class.} \end{cases} \tag{2.36}$$

By solving Eq. (2.28) numerically, approximate critical points $U_N^\star$ are obtained for hard hexagons and squares, as listed in TABLE 2.4. In the case of hard hexagons, the approximate critical point converges very rapidly to the exact value as $O(N^{-3.2})$. According with the fact that $y_t = 6/5$ (for the three-state Potts universality class), this asymptotic behavior indicates that the leading correction to the scaling dimension x_σ is $O(N^{-2})$, although the conformal perturbation theory [47] predicts a non-analytic leading correction $N^{-0.8}$ for the three-state Potts universality class. In fact, the effective

*For example, it gives $U_c = \log 4 = 1.386\cdots$ for hard squares. Compare with Eq. (2.35).

N	$U_N^\star$	$x_{\sigma,N}$
3	2.240170985	0.11684608545
6	2.378530393	0.12736576823
9	2.397538174	0.13036422387
12	2.402481675	0.13158077208
15	2.404259779	0.13218369276
18	2.405039548	0.13252356304
21	2.405430545	0.13273310046
24	2.405646500	0.13287106317
27	2.405774813	0.13296657907
∞	2.4060589(4)	0.133333333(1)
exact	$2.406059125\cdots$	2/15

N	$U_N^\star$	$x_{\sigma,N}$
6	1.3300827976	0.119649638
8	1.3323468767	0.124464413
10	1.3331634433	0.124659219
12	1.3335246144	0.124764845
14	1.3337077370	0.124828233
16	1.3338101154	0.124869154
18	1.3338717053	0.124897065
20	1.3339109298	0.124916935
22	1.3339370745	0.124931574
24	1.3339551618	0.124942666
26	1.3339680687	0.124951268
28	1.3339775233	0.124958073
∞	1.33401512(2)	0.1250000(1)
Ising	—	1/8

TABLE 2.4. Approximate critical point $U_N^\star$ and effective leading scaling dimension $x_{\sigma,N}$ of hard hexagons (left) and squares (right) by using the transfer matrices of type (a) and (b), respectively.

leading scaling dimension at the *exact* critical point U_c,

$$x_{\sigma,N} = \frac{N}{2\pi\zeta\xi_N(U_c)} , \tag{2.37}$$

converges to the exact value 2/15 as $O(N^{-2})$, as seen in TABLE 2.4.

In the case of hard squares, the convergence of the approximate critical point is also quite rapid ($O(N^{-3})$). This convergence is an indication that the correct value of x_σ is used. By using the BST extrapolation algorithm [48] with $\omega = 3.0$, we obtained†

$$U_c = 1.33401512(2) , \tag{2.38}$$

which coincides well with the previous estimate (2.35). The effective scaling dimension $x_{\sigma,N}$ at $U = U_c$ also converges to the expected value 1/8 as $O(N^{-2})$.

†Of course, there are many other schemes for sequence extrapolation: Shanks' method [49], Levin's method [50], VBS algorithm [51], *etc.* However, in general, the BST algorithm converges faster and produces more reliable estimates [52]. For reviews on extrapolation algorithms, see [53–56].

2.5. Interacting Hard Hexagons

2.5.1. Transitions in Regions II and III. For the next-nearest-neighbor attraction ($W_2 > 0$), there exists a transition *line*, which connects the critical point of non-interacting hard hexagons [33]:

$$(W_2, U) = \left(0, \log\frac{11+5\sqrt{5}}{2}\right) = (0, 0.2406059125\cdots) \tag{2.39}$$

and the ground-state phase transition point:

$$(W_2, U) = (\infty, -\infty) \quad \text{with } U/W_2 = -3\ . \tag{2.40}$$

As is seen in FIGURE 2.6, for sufficiently small W_2, the effective thermal exponent $y_{t,L}$ (Eq. (2.31)) seems to converge to that of the three-state Potts model ($y_t = 6/5$). On the other hand, it diverges for $W_2 \gtrsim 1$. This behavior indicates that a first-order transition occurs for $W_2 \gtrsim 1$ instead of a second-order transition of the three-state Potts universality. In other words, there exists a tricritical point.

To locate the tricritical point, which is expected to belong to the tricritical three-state Potts universality class ($c = 6/7$), we estimate a density gap associated with a first-order transition directly by the same technique as in [57–59] (for details, see section 3.4). We calculate an effective density gap of the finite system:

$$\Delta\rho_N = [(\langle 0|\hat{\rho}|0\rangle - \langle\epsilon|\hat{\rho}|\epsilon\rangle)^2 + 4\langle 0|\hat{\rho}|\epsilon\rangle^2]^{1/2}\ . \tag{2.41}$$

at the approximate critical point U_N^*. Here, $\hat{\rho}$ is the density operator, and $|0\rangle$ and $|\epsilon\rangle$ are the eigenvectors corresponding to the largest and fourth-largest eigenvalues, which are both *even* under cyclic translations of the lattice sites. For a transition of second order, the above effective density gap is expected to vanish in the thermodynamic limit as $O(N^{-(1-\alpha)/\nu})$, where

$$\frac{1-\alpha}{\nu} = \begin{cases} 4/5 & \text{for } c = 4/5, \\ 2/7 & \text{for } c = 6/7. \end{cases} \tag{2.42}$$

For a first-order transition, it remains finite for $N \to \infty$. We extrapolate the effective density gap by using the BST algorithm with $\omega = 4/5$ and $2/7$ (FIGURE 2.7). For small W_2, the extrapolation with $\omega = 4/5$ leads to the expected result $\Delta\rho \simeq 0$. However, near the tricritical point it gives a finite density gap with large error of estimate, which may be due to a crossover effect to the tricritical three-state Potts universality. On the contrary, the extrapolation with $\omega = 2/7$ over-estimates in the $c = 4/5$ region, and causes a change of sign in the estimate of the density gap close to the tricritical point (FIGURE 2.7). Thus, we obtain a location of the tricritical point as

$$(W_2, U)_t = (0.935(3), -2.61(1))\ . \tag{2.43}$$

2.5.2. Transition in Region IV. In this region the $\sqrt{3}\times\sqrt{3}$ and 2×2 phases appear owing to the competing repulsive W_2 and positive U. First we consider the hard-core limit, e.g. $W_2 \to -\infty$. This limit has been studied by Orban and Bellemans [60] and Runnels, *et al.* [61]. They concluded a first-order phase transition to the 2×2 phase.

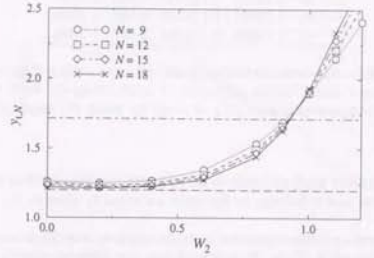

FIGURE 2.6. Effective thermal exponent $y_{t,N}$ along the $\sqrt{3}\times\sqrt{3}$ phase boundary for $N = 9, 12, 15, 18$ in terms of the type (d) transfer matrix. The horizontal line denotes the thermal exponent expected for the three-state Potts (dashed line, $y_t = 6/5$) and tricritical three-state Potts (dot-dashed line, $y_t = 12/7$) universality class, respectively.

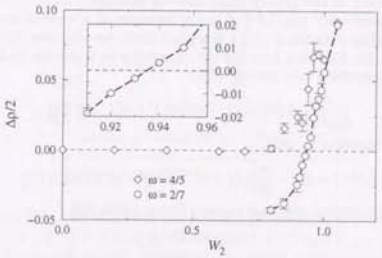

FIGURE 2.7. Density gap along the $\sqrt{3}\times\sqrt{3}$ phase boundary extrapolated by the BST algorithm with $\omega = 4/5$ (diamond) and $\omega = 2/7$ (circle) by using the type (d) transfer matrix for $N = 9, 12, \cdots, 24$.

N	U_N^*	$x_{\sigma,N}$	c_N	$y_{t,N}$
12	1.76293	0.113076	0.982	1.4319
16	1.76498	0.112528	0.976	1.4020
20	1.76252	0.113432	0.983	1.3941
24	1.76086	0.114219	0.988	1.3958
28	1.75989	0.114794	0.987	1.4000

TABLE 2.5. Approximate critical point, effective scaling dimension, central charge, and thermal exponent of hard hexagons with the next-nearest-neighbor exclusion ($W_2 \to -\infty$) by using the type (g) transfer matrix.

However, the present analysis leads to an opposite conclusion, that is, the transition is of second order and it belongs to the same universality class as the four-state Potts model.

The approximate critical point U_N^* is obtained by the phenomenological renormalization (2.29) with $N' = N + 4$ by using the transfer matrix of type (g) for $N = 4, 8, \cdots, 28$. The results are listed in TABLE 2.5. An extrapolation to the thermodynamic limit yields [62]

$$U_c = 1.756(1), \tag{2.44}$$

which agrees with the previous estimate $U_c = 1.750(5)$ [60].

The leading scaling dimension and the thermal exponent can be also estimated as $x_\sigma \simeq 0.116$ and $y_t \simeq 1.40$, respectively [62]. These results slightly differ from that of the four-state Potts universality class ($x_\sigma = 1/8$ and $y_t = 3/2$), which is expected from the degeneracy of the ground state and the symmetry of the order parameter. However, this discrepancy may be due to the presence of a logarithmic correction to the finite-size scaling associated with a marginal irrelevant operator [63].

If we assume the following forms of the correction to finite-size scaling by taking the logarithmic correction into account [63]:

$$\frac{L}{\xi_N(U_c)} = 2\pi\zeta x_\sigma\{1 + a/\log N + o(1/\log N)\} \tag{2.45}$$

for the scaling dimension x_σ and

$$f_L(U_c) = f_\infty - \frac{\pi\zeta}{6N^2}\{c + b/(\log N)^3 + o(1/(\log N)^3)\} \tag{2.46}$$

for the free-energy density, the least-squares fitting yields [62]

$$x_\sigma = 0.125(2) \tag{2.47}$$

$$c = 1.00(1)\,. \tag{2.48}$$

These estimates exhibit good agreements with the expected values $x_\sigma = 1/8$ and $c = 1$. Consequently, we conclude that the transition is of second order in the four-state Potts universality class [62].

For finite but negative W_2, on the other hand, three kinds of transition line appear, the disordered–$(\sqrt{3}\times\sqrt{3})$, disordered–(2×2), and $(\sqrt{3}\times\sqrt{3})$–(2×2) coexistence lines.

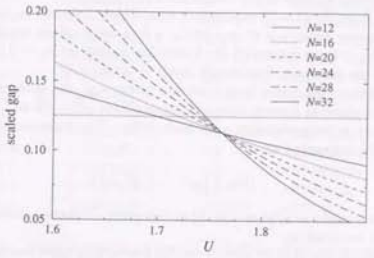

FIGURE 2.8. The scaled gap of hard hexagons with the next-nearest-neighbor exclusion ($W_2 \to -\infty$) by using the type (g) transfer matrix. The horizontal dotted line denotes that of the four-state Potts universality class ($x_\sigma = 1/8$).

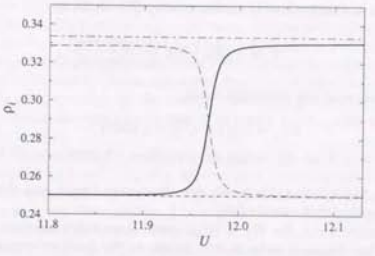

FIGURE 2.9. Derivatives of the free-energy levels, $\rho_i = -\partial f_i/\partial U$, near the $\sqrt{3}\times\sqrt{3}$ – 2×2 coexistence line for $N = 12$ and $W_2 = -1.0$. Each line corresponds to the 'density' of the stable state (thick solid line), metastable state (long-dashed line), $\sqrt{3}\times\sqrt{3}$ state (dot-dashed line), and the 2×2 state (dashed line), respectively.

The first one is shown to be the three-state Potts universality class. Similarly, the second one belongs to that of the four-state Potts model.

On the $(\sqrt{3}\times\sqrt{3})$–(2×2) coexistence line, which is found to be very close to the ground-state phase boundary $U=-12W_2$, a first-order phase transition occurs. For example, at $W_2=1$, we estimated the transition density as $\rho_\pm = 0.29\pm 0.04$ from the derivatives of the dominant free-energy levels (FIGURE 2.6).

The above three transition lines meet at a point, e.g., the *multicritical point*, where one disordered phase and seven ordered phases (three $\sqrt{3}\times\sqrt{3}$ and four 2×2 ordered phases) become indistinguishable with each other. The location of this multicritical point is roughly estimated as

$$(W_2, U)_{\rm m} = (-0.59, 7.1)\,. \tag{2.49}$$

It is naively expected $c=9/5\,(=4/5+1)$ at this point. However, it remains inconclusive in the present calculation.

We summarize the present results on the interacting hard-hexagon model in FIGURE 2.14 on p. 28.

2.6. Interacting Hard Squares

2.6.1. Transition to the $\sqrt{2}\times\sqrt{2}$ Phase. For sufficiently large next-nearest-neighbor attraction W_2 (>0), the transition to the $\sqrt{2}\times\sqrt{2}$ phase is of first order as same as in the case of the $\sqrt{3}\times\sqrt{3}$ phase boundary of interacting hard hexagons. In this case, the first-order transition line is known exactly [33, 64, 65] as

$$U = -2W_2 + \log\frac{(1-\exp W_2)^2}{1-2\exp W_2}\,, \tag{2.50}$$

and it terminates at the *tricritical* point:

$$\begin{aligned} W_{2,{\rm t}} &= \log(3+\sqrt{5}) = 1.65557\cdots \\ U_{\rm t} &= \log(\sqrt{5}-1)/32 = -3.25380\cdots\,. \end{aligned} \tag{2.51}$$

On this line, the interfacial tension, the correlation length and the sublattice-density gap are also calculated exactly [66].

On the other hand, for $W_2 < W_{2,{\rm t}}$, there is no exact solution. The transition is expected to be of second order and to belong to the Ising universality class [67]. This critical line is determined accurately by solving Eq. (2.28) with $x_\sigma = 1/8$ numerically. In the whole region ($W_2 < W_{2,{\rm t}}$), the approximate critical point exhibits a good convergence of $O(N^{-3})$. Thus, the critical line $U=U_{\rm c}(W_2)$ are obtained up to 7 digits or more, as shown in TABLE 2.6. In contrast to the case on the triangular lattice, the $\sqrt{2}\times\sqrt{2}$ phase does *not* come in contact with the 2×1 phase at finite temperatures. In the limit $W_2\to-\infty$, the phase boundary asymptote is estimated to be

$$U_{\rm c}(W_2) = -4W_2 + 0.84650(1)\,. \tag{2.52}$$

W_2	$U_{\rm c}(W_2)$	W_2	$U_{\rm c}(W_2)$
-15.0	60.846506(3)	0	1.33401512(2)
-10.0	40.846525(3)	0.2	0.6565480(1)
-5.0	20.849429(3)	0.4	0.0093342(5)
-4.0	16.854457(3)	0.6	-0.6032717(1)
-3.0	12.868158(3)	0.8	-1.17856740(3)
-2.0	8.905729(2)	1.0	-1.7162027(2)
-1.5	6.9449653(2)	1.2	-2.218293(2)
-1.0	5.0115774(9)	1.3	-2.457246(8)
-0.8	4.2502484(7)	1.4	-2.68901(3)
-0.6	3.4987005(4)	1.5	-2.91438(9)
-0.4	2.7596833(1)	1.6	-3.1343(2)
-0.2	2.0366945(1)	1.65557$\cdots$	-3.25380$\cdots$

TABLE 2.6. Phase boundary of the $\sqrt{2}\times\sqrt{2}$ phase of the interacting hard squares in terms of the transfer matrix of type (b) with $N=2,4,\cdots,20$ except for $W_2=0$ ($N_{\rm max}=28$) and $W_2=1.65557\cdots$ (exact solution [33, 64, 65]).

2.6.2. Transition to the 2×1 Phase. The transition to the 2×1 phase has also been investigated by Kinzel and Shick [67]. They used the *row-to-row* transfer matrices (type (e) in TABLE 2.3) up to $N=14$, and concluded the existence of a *non-universal* transition line. That is, the thermal exponent varies continuously along the transition line. Especially, for $W_2\to-\infty$, they concluded $U=4.70$ and $y_{\rm t}=0.925$.

In general, the physical consequences obtained by the transfer matrices are expected to be independent of the way to choose a transfer direction. In fact, the previous results in this chapter do not dependent on the transfer direction. However, in this case, two different transfer directions lead to completely different results with respect to each other.

In the case of the *row-to-row* transfer matrix (type (e)), as is seen clearly in TABLE 2.7 and FIGURES 2.10 and 2.11, the approximate critical point U_N^* increases as the system size increases, and seems to diverge for $N\to\infty$. In addition, the effective scaling dimension $x_{\sigma,N}$ vanishes rapidly. The effective central charge c_N and the $y_{{\rm t},N}$ also do not seems to converge to any finite limits.

On the contrary, in the case of the *diagonal-to-diagonal* transfer matrix (type (f)), the situation is completely different (TABLE 2.7 and FIGURE 2.12). The approximate critical point U_N^* *decreases* as the system size increases, that is, the ordered phase extends wider and wider by improving the degrees of approximation. It seems to converge to $U_{\rm c}\simeq 4.65$. The other quantities, $x_{\sigma,N}$, c_N, and $y_{{\rm t},N}$, also seem to remain at finite values, although they have extremely slow convergence.

The results in terms of different transfer directions contradict completely with each other. The first one indicates that there is no phase transition, and the second one persists the existence of a phase transition at a finite chemical potential. However, we support the second one. The reason is the following:

N	U_N^*	$x_{\sigma,N}$	c_N	$y_{t,N}$
6	4.39512	0.023247	2.1340	0.90606
8	4.55192	0.017835	2.5912	0.92959
10	4.70119	0.012918	3.0056	0.93388
12	4.83561	0.009037	3.3867	0.92035
14	4.95579	0.006180	3.7390	0.89223
16	5.06419	0.004158	4.0658	0.85332
18	5.16332	0.002763	4.3696	0.80730
20	5.25521	0.001816	4.6533	0.75752
22	5.34131	0.001183	4.9191	0.70687
24	5.42243	0.000766	5.1688	0.65760
26	5.49878	0.000496	5.4170	0.59132

N	U_N^*	$x_{\sigma,N}$	c_N	$y_{t,N}$
12	4.82924	0.058470	0.47002	0.47848
16	4.83394	0.058254	0.52393	0.49634
20	4.80980	0.059513	0.56221	0.53615
24	4.77869	0.061366	0.59072	0.58594
28	4.75048	0.063283	0.61253	0.63632
32	4.72729	0.065068	0.63007	0.68299

TABLE 2.7. Approximate critical point U_N^*, effective leading scaling dimension $x_{\sigma,N}$, central charge c_N, and thermal exponent $y_{t,N}$ of hard squares with next-nearest-neighbor exclusion ($W_2 \to -\infty$), by means of the row-to-row (type (e), upper) and diagonal-to-diagonal (type (f), lower) transfer matrices, respectively.

As is discussed in section 2.2, only the four-sublattice symmetry is broken in the 2×1 phase, but the two-sublattice one is conserved. Consequently, the eigenvector corresponding to the breaking of the present symmetry must be *even* under the exchange of two sublattices, while that of the row-to-row transfer matrix is *odd* under such a transformation. Moreover, on the unit slice (α) in FIGURE 2.4, which is used for the row-to-row transfer matrix, we can not define any order parameter which corresponds to the four-sublattice symmetry breaking. Thus, our first result is not an indication of the non-existence of the 2×1 phase, but that of the $\sqrt{2}\times\sqrt{2}$ or 2×2 phases in this limit[‡] ($W_2 \to -\infty$).

[‡]It should be noted that a similar situation occurs in the case of the antiferromagnetic transition of the restricted solid-on-solid (RSOS) model, where the ordered phase has $r\times1$ structure [68–70].

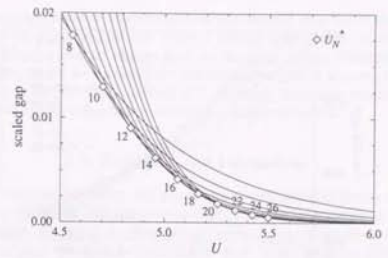

FIGURE 2.10. Scaled gap of hard squares with the next-nearest-neighbor exclusion ($W_2 \to -\infty$) by using the *row-to-row* transfer matrix (type (e)). The approximate critical points U_N^* are denoted by diamonds.

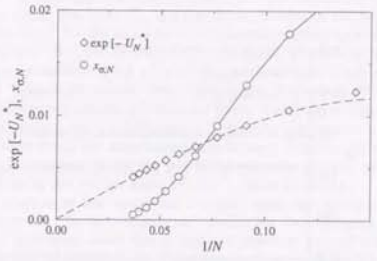

FIGURE 2.11. Size dependence of the approximate critical point U_N^* (diamond) and the effective scanling dimension $x_{\sigma,N}$ (circle) of hard squares with the next-nearest-neighbor exclusion ($W_2 \to -\infty$) by using the *row-to-row* transfer matrix (type (e)). Note that the approximate critical point is plotted as $\exp[-U_N^*]$. The solid and dashed lines are merely guides to eyes.

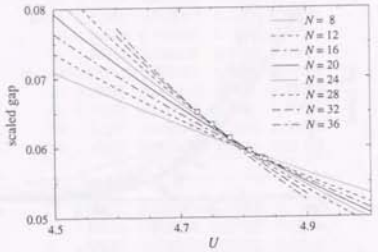

FIGURE 2.12. Scaled gap of hard squares with the next-nearest-neighbor exclusion ($W_2 \to -\infty$) by using the *diagonal-to-diagonal* transfer matrix (type (f). The fixed points of the phenomenological renormalization are denoted by diamonds.

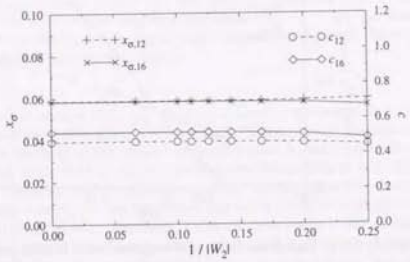

FIGURE 2.13. Effective central charge and leading scaling dimension of the repulsive hard squares along the 2×1 phase boundary.

Thus, we conclude that a second-order transition occurs at $U \simeq 4.65$. The other critical parameters are also estimated as $c = 0.8 \sim 1.0$, $x_\sigma = 0.8 \sim 1.0$, and $y_t = 0.9 \sim 1.2$.

For the finite next-nearest-neighbor interaction, we can also obtain the phase boundary by using the *diagonal-to-diagonal* transfer matrix as shown in FIGURE 2.15. Along this line, the effective central charge and the leading scaling dimension remain unchanged (FIGURE 2.13). So we conclude this transition line is *universal*, in contrast to the previous result by Kinzel and Schick [67]. However, a precise determination of the universality class of this transition remains as a future problem.

2.7. Summary and Discussions

In the present chapter, we study the two-dimensional classical lattice gases with the nearest-neighbor exclusion and the next-nearest-neighbor interaction on the triangular and square lattices. By using the dimensional reduction and the sparse-matrix factorization, we calculated the transfer matrix for quite larger systems than the previous works. In the absence of the next-nearest-neighbor interaction ($W_2 = 0$), our results on the triangular and square lattices exhibit excellent agreements with the exact solution and with the expected values for the Ising universality class, respectively.

For finite next-nearest-neighbor interaction, we found the quantitative phase diagrams (FIGURES 2.14 and 2.15). In the case of the next-nearest-neighbor attraction ($W_2 > 0$), these phase diagrams are qualitatively the same with each other. That is, for sufficient small W_2, these systems undergo a second-order transition, which terminates at the tricritical point. For large W_2, the transition changes to the first-order one.

On the other hand, for the repulsive next-nearest-neighbor interaction ($W_2 < 0$), their phase diagrams are quite different with each other. In the case of the triangular lattice, the phase boundaries of the $\sqrt{3} \times \sqrt{3}$ phase (three-state Potts universality) and that of the 2×2 phase (four-state Potts universality [62]) meet at the multicritical point. Between these two phases, a first-order phase transition occurs.

On the square lattice, the $\sqrt{2} \times \sqrt{2}$ and 2×1 phase do not come in contact with each other. There always exists the disordered phase between them for finite temperatures. In contrast to the previous works, we concluded that the critical exponent or other critical parameters do not change along the 2×1 phase boundary.

Finally, we summarize the results for the *pure* hard-core lattice gases up to the present in TABLE 2.8. In two dimensions, except for hard squares with the next-nearest-neighbor exclusion, which has a highly degenerate ground state, the second-order transitions can be classified into the corresponding Potts models in terms of the ground-state degeneracy.

On the other hand, in three dimensions, the nearest-neighbor model on the simple cubic lattice (hard-sphere lattice gas) has been indicated to belong a different universality class from that of the three-dimensional ferromagnetic Ising model by Monte Carlo simulations [71, 72]. It remains as an interesting future problem.

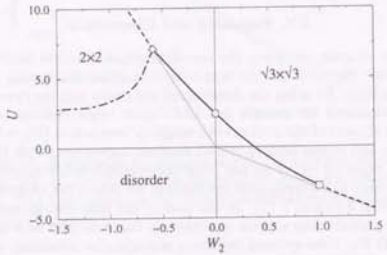

FIGURE 2.14. Phase diagram of interacting hard hexagons. The solid and dot-dashed lines denote the second-order-transition line of $c = 4/5$ and $c = 1$, respectively. The dashed lines denote the first-order transition. The non-interacting point (Eq. (2.34)) and the multicritical points (Eqs. (2.49) and (2.43)) are denoted by the circle, square, and the diamond, respectively. The thin dotted line denotes the low-temperature limit ($U = -3W_2$ for $W_2 > 0$ and $U = -12W_2$ for $W_2 < 0$).

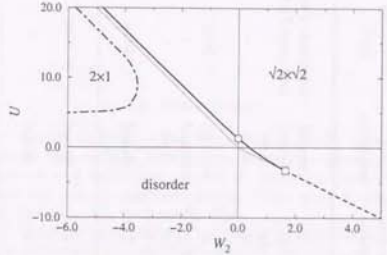

FIGURE 2.15. Phase diagram of interacting hard squares. The solid and dot-dashed lines denote the second-order-transition line of $c = 1/2$ and $c = 0.8 \sim 1.0$, respectively. The dashed line denotes the first-order transition. The non-interacting point (Eq. (2.38)) and the tricritical point (Eq. (2.51)) are denoted by the circle and the diamond, respectively. The thin dotted line denotes the low-temperature limit ($U = -2W_2$ for $W_2 > 0$ and $U = -4W_2$ for $W_2 < 0$).

lattice	exclusion range	U_c	ground-state degeneracy	order of transition	universality class	references
triangular	1	2.406051925 ⋯	3	second	three-state Potts	[33], section 2.4
	2	1.756(1)	4	second	four-state Potts	[62], section 2.5
	3	4.7	14	first	—	[60,61]
	4	2.90	9	first	—	[60]
square	1	1.334015104(8)	2	second	Ising	[44,45], section 2.4
	2	4.65	$4 \times 2^{\sqrt{5}/2}$	second	?	section 2.6
	3	3.64	10	first	—	[43]
hexagonal	1	2.06073285(3)	2	second	Ising	[31]
simple cubic	1	0.0571(3)	2	second	≠ Ising ?	[71,72]
body centered cubic	1	−0.3253(4)	2	second	?	[73]

TABLE 2.8. Transitions of the *pure* hard-core lattice gases.

CHAPTER 3

Quantum Hard Rods

3.1. Introduction

In the present chapter we study a one-dimensional quantum system. Van Hove's theorem [74] states that at finite temperatures there is no phase transition in one-dimensional systems with finite-range interaction. However, non-trivial ground-state phase transitions may occur in quantum systems. These phase transitions are caused not by thermal fluctuation but by quantum effect.

A system of "quantum hard rods" was introduced by Iglói [75] as a quantum analogy for classical models with near-neighbor exclusion describing the solid–fluid phase transitions. The Hamiltonian of this system is defined as*

$$\mathcal{H}^{(m)} = -\mu \sum_{i=1}^{L} \sigma_i^z - \sum_{i=1}^{L} \sigma_i^x + \sum_k \left\{ J_k \sum_{i=1}^{L} (\sigma_i^x + 1)(\sigma_{i+k}^x + 1) \right\}, \tag{3.1}$$

where σ_i^x and σ_i^z are Pauli matrices at site i, and $J_k = \infty$ for $k = 1, 2, \ldots, m-1$ and $J_k = 0$ for $k \geq m$. Owing to the presence of the infinite repulsion up to $(m-1)$th-nearest neighbors, two *up* spins are separated at least by a distance of m. Thus, a hard rod with length m is assigned to each up spin. The longitudinal field μ, which corresponds to the chemical potential of the classical models, controls the density of hard rods.

This system can be considered as a special limit of a multispin-coupling model with longitudinal and transverse fields:

$$\mathcal{H}_M^{(m)} = (-1)^m \sum_{i=1}^{L} \prod_{k=1}^{m} \sigma_{i+k-1}^x - h_\ell \sum_{i=1}^{L} \sigma_i^z - h_t \sum_{i=1}^{L} \sigma_i^x. \tag{3.2}$$

If we take a limit $h_\ell \to -m$ and $h_t \to 0$ with $\mu = (h_\ell + m)/h_t$ fixed, the Hamiltonian of quantum hard rods, Eq. (3.1), is obtained.

*Note that for the consistency with the previous chapters, our definition of the Hamiltonian is slightly different from that introduced by Iglói [75]. The Hamiltonian and field in out notation can be expressed as $\mathcal{H}(\mu) = H(h)/h$ and $\mu = 1/h$ by those used in [75].

The multispin-coupling Hamiltonian (3.2) for $h_t = 0$ has been quite well studied analytically and also numerically. For any m (≥ 2), a phase transition should occur at $h_t = 1$ due to the self duality of the Hamiltonian [76,77]. In the ordered phase ($h_t < 1$) the ground state has 2^{m-1}-fold degeneracy, and the transition is of second order for $m = 2$ (Ising universality) [78] and for $m = 3$ (four-state Potts universality) [79–82], while it is of first order for $m \geq 4$ [83,84]. In the presence of a negative longitudinal field, the ground-state degeneracy of the ordered phase changes to m. Thus, along the phase boundary, which connects $(h_t, h_l) = (0, 1)$ and $(-m, 0)$, one expects for $m \geq 3$ a class of universality different from that for $h_t = 0$. Penson *et al.* [85] have studied the $m = 3$ system and found a phase transition of the three-state Potts model universality class in accordance with the ground-state degeneracy of the ordered phase. However, fluctuations in the numerical data were so strong for $-3 < h_t \lesssim -2$ that no conclusion could be made in this region.

In the hard-core limit, the Hamiltonian (3.1) has been studied by the exact diagonalization [75] for $m = 2$ and 3, and by the quantum Monte Carlo simulation [86] for $m = 2$, 3, 4, and 5. For $m = 2$, they found a second-order transition of the Ising universality class [75, 86], which is expected to be so from the consideration of the ground-state degeneracy. On the other hand, for $m \geq 4$, the energy distribution function at the critical point exhibits clear double peaks [86] and the first-order transition was concluded. For $m = 3$, they concluded a transition of weakly first order due to the presence of a finite but quite small latent heat ($\Delta L = 0.004(4)$) [75]. However, it is comparable with the error of the estimate, so the possibility of a second-order transition cannot be excluded.

In the present chapter, we study the quantum hard-rod model (3.1) in the same exact-diagonalization method as in the previous work by Iglói [75]. We perform diagonalization for quite larger systems ($L_{\max} = 30$ and 42 for $m = 2$ and 3, respectively), while they have calculated up to $L_{\max} = 22$ and 30, respectively. In addition, we also investigate the model for $m = 4$, 5, 6, and 7 using our improved algorithm, which has made possible accurate estimation, and calculate the density gap, or equivalently the latent heat, which are associated with the first-order transition.

3.2. Exact Diagonalization

While the dimension of the eigenvalue matrix corresponding to the multispin-coupling model (3.2) is given by 2^L, that of the hard-rod Hamiltonian (3.1) is extremely reduced due to the presence of the near-neighbor exclusion as in the case of the transfer matrices for the two-dimensional classical hard-core lattice gases discussed in the last chapter. The effective dimension of our eigenvalue matrix is given by

$$d_m(L) \simeq x_m^L \tag{3.3}$$

for $L \gg 1$, where L is the size of the system and x_m is the maximum solution of the following equation:

$$x^m - x^{m-1} - 1 = 0\,. \tag{3.4}$$

For example, $x_2 = 1.61803$ and $x_3 = 1.46557$. For details, see appendix B.

If we restrict ourselves to this highly reduced space, referred to as $\psi_m^{(\mathrm{p})}(L)$ in appendix B, the exclusion rule, caused by the third term of *r.h.s.* in Eq. (3.1), is always satisfied. Consequently, the Hamiltonian can be reduced to the following effective non-interacting Hamiltonian:

$$\tilde{\mathcal{H}} = -\mu \sum_{i=1}^{L} \sigma_i^z - \sum_{i=1}^{L} \sigma_i^x\,. \tag{3.5}$$

Thus, the multiplication of the eigenvalue matrix to a trial vector can be coded quite simply. By using the Lanczos diagonalization algorithm [28–30], dominant eigenvalues and the corresponding eigenvectors are calculated efficiently. This is one of the great merits in our method.

3.3. Phenomenological Renormalization

In terms of the lowest and second-lowest eigenvalues, E_0 and E_1, of the eigenvalue matrix, the correlation length corresponding to the order–order correlation function is given by $\xi_L^{-1} \sim E_1 - E_0$. The finite-size scaling [19–21,26,27] states that the *scaled gap* at the critical point,

$$g_L = L(E_1(L) - E_0(L))\,, \tag{3.6}$$

tends towards a constant, and consequently, an approximate critical point can be obtained as a fixed point of the phenomenological-renormalization mapping [22–25], that is,

$$g_L(\mu_L^*) = g_{L'}(\mu_L^*) \tag{3.7}$$

for different system sizes, L and L'. Moreover, according to the conformal invariance [15–18], it has a *universal* value up to an unknown factor ζ:

$$g_L(\mu) = 2\pi\zeta x_\sigma \tag{3.8}$$

for $\mu \to \mu_c$ and $L \to \infty$, where x_σ is the scaling dimension of the corresponding correlation function. This factor ζ, referred to as the *sound velocity*, must be introduced owing to the anisotropy in the real-space and imaginary-time directions. Although it is determined by the lattice shape and the way of transferring in the transfer-matrix formalism of two-dimensional classical systems [32], in general, it can *not* be determined beforehand in the case of one-dimensional quantum systems. It must be fixed by means of finite-size data. The ground-state energy also has a universal finite-size correction:

$$\frac{E_0(L)}{L} = \epsilon_0 - \frac{\pi\zeta c}{6L^2} + \cdots \tag{3.9}$$

for periodic boundary conditions, where c is the central charge and ϵ_0 is the ground-state-energy density of the bulk.

The thermal exponent y_t can be calculated, using the scaling law:

$$\left.\frac{dg_L(\mu)}{d\mu}\right|_{\mu=\mu^*} \simeq aL^{y_t}\,. \tag{3.10}$$

L	μ_L^*	$g_L(\mu_L^*)$	$y_{t,L}$	$(x_\sigma/c)_L$
6	0.646896253	1.4978913	1.066477	0.24821601
8	0.651479452	1.4725914	1.044559	0.24873377
10	0.653191715	1.4607752	1.032887	0.24906901
12	0.653972728	1.4542998	1.025796	0.24929083
14	0.654378843	1.4503664	1.021093	0.24944336
16	0.654610609	1.4477980	1.017773	0.24955214
18	0.654752413	1.4460284	1.015320	0.24963219
20	0.654844002	1.4447573	1.013439	0.24969271
22	0.654905777	1.4438136	1.011958	0.24973953
24	0.654948947	1.4430937	1.010760	0.24977647
26	0.654980022	1.4425321	1.009775	0.24980610
28	0.655002959	1.4420854	1.008952	0.24983023
∞	0.6550966(1)	1.439260(2)	1.0000(1)	0.249998(3)

TABLE 3.1. Fixed point of the phenomenological renormalization μ_L^*, effective scaled gap $g_L(\mu_L^*)$, effective thermal exponent $y_{t,L}$, and effective scaling dimension ratio $(x_\sigma/c)_L$ for $m = 2$. Their extrapolated values to $L \to \infty$ are also listed.

In practice, we consider an *effective* thermal exponent $y_{t,L}$, obtained by

$$y_{t,L} = \left\{ \log \left(\frac{dg_{L'}}{d\mu} \Big/ \frac{dg_L}{d\mu} \right)_{\mu=\mu_L^*} \right\} \Big/ \log(L'/L) . \tag{3.11}$$

We have also calculated a *ratio* of the effective scaling dimension:

$$x_{\sigma,L} = \frac{g_L(\mu_L^*)}{2\pi\zeta} \tag{3.12}$$

and the effective central charge:

$$c_L = \left. \frac{6LL'(LE_0(L') - L'E_0(L))}{\pi\zeta(L'^2 - L^2)} \right|_{\mu=\mu_L^*} \tag{3.13}$$

to get rid of the uncertainty due to the unknown factor ζ.

Results for $m = 2$. In this case, we have diagonalized the eigenvalue matrix up to $L = 30$. Due to the antiferromagnetic-like order, only even L $(= 2, 4, 6, \cdots, 30)$ are used in the finite-size analysis. An approximate critical point is calculated by Eq. (3.7) with $L' = L + 2$. As shown in TABLE 3.1, the approximate critical point μ_L^* converges to its limit rapidly as $O(L^{-3})$. By using the BST algorithm [48] with $\omega = 3.0$, we obtained

$$\mu_c = 0.6550966(1) , \tag{3.14}$$

which is more accurate than the previous estimate $\mu_c = 0.655097(2)$ by Iglói [75]. The effective thermal exponent and the ratio of the scaling dimension and the central charge also exhibit good convergence, and we obtained

$$y_t = 1.0000(1) \tag{3.15}$$

and

$$x_\sigma/c = 0.249998(3) , \tag{3.16}$$

by means of the BST algorithm with $\omega = 1.0$ and 2.0, respectively. These estimates agree excellently with the exact value of the Ising universality class:

$$y_t = 1 , \; c = \frac{1}{2} , \text{ and } \; x_\sigma = \frac{1}{8} . \tag{3.17}$$

The value of the scaled gap converges to 1.439260(2). If we assume that this transition actually belongs to the Ising universality, we can estimate the sound velocity as

$$\zeta = 1.832523(3) , \tag{3.18}$$

by using Eq. (3.12) and $x_\sigma = 1/8$.

Results for $m = 3$. In this case, we have calculated up to $L = 42$. The maximum dimension of the corresponding eigenvalue matrix is about 9.4×10^6. Only $L = 3, 6, 9, \cdots, 42$ are compatible with the ordered state configuration. In contrast to the $m = 2$ case, the convergence of the critical point, obtained by Eq. (3.7) with $L' = L + 3$, is at most $O(L^{-1})$. By extrapolating them to $L \to \infty$, we obtained

$$\mu_c = 0.98719(3) . \tag{3.19}$$

For relatively small L, the effective thermal exponent $y_{t,L}$ seems to converge to ~ 1.32. However, it tends to diverge as L becomes larger, as seen in FIGURE 3.1. On the other hand, the scaled gap at the approximate critical point apparently vanishes in the $L \to \infty$ limit (FIGURE 3.2). Thus, we conclude the $m = 3$ model exhibits a first-order

L	μ_L^*	$g_L(\mu_L^*)$	$y_{t,L}$
6	0.8669274	2.49007	1.36935
9	0.9096687	2.19630	1.33309
12	0.9281706	2.02543	1.32445
15	0.9389431	1.89961	1.32465
18	0.9461596	1.79749	1.32844
21	0.9513954	1.71043	1.33388
24	0.9553949	1.63404	1.34016
27	0.9585625	1.56575	1.34686
30	0.9611400	1.50389	1.35379
33	0.9632817	1.44731	1.36081
36	0.9650918	1.39516	1.36794
39	0.9666433	1.34678	1.37501

TABLE 3.2. Fixed point of the phenomenological renormalization μ_L^*, effective scaled gap $g_L(\mu_L^*)$, and effective thermal exponent $y_{t,L}$ for $m = 3$.

transition, and the spurious convergence of y_t for small L may be due to the crossover effect to the three-state Potts model ($y_t = 6/5$) [87].

Results for $m \geq 4$. For $m = 4$, 5, 6, and 7, we have calculated up to $L = 36$, 40, 42, and 49, respectively. Approximate critical points are obtained by Eq. (3.7) with $L' = L + m$, in the same way as in the previous cases. These approximate critical points converge to

$$\mu_c = \begin{cases} 1.2328(1) & \text{for } m = 4 \\ 1.429(2) & \text{for } m = 5 \\ 1.575(5) & \text{for } m = 6 \\ 1.749(1) & \text{for } m = 7 \end{cases} \tag{3.20}$$

as $O(L^{-1})$. As is seen apparently in FIGURES 3.1 and 3.2, the effective thermal exponent diverges and the scaled gap vanishes more quickly as m increases. Consequently, all the transitions are of first order as in the case for $m = 3$.

3.4. Density Gap

Next we evaluate a density gap, which should be associated with a first-order transition, directly. The lowest eigenvalue E_0 has an eigenstate $|0\rangle$, which is *even* under cyclic translations. For finite L, only E_0 contributes to the density of hard rods:

$$\begin{aligned} \rho &= \frac{1}{2} - \frac{1}{2L}\frac{dE_0}{d\mu} \\ &= \langle 0|\hat{\rho}|0\rangle , \end{aligned} \tag{3.21}$$

where $\hat{\rho}$ is the density operator defined by

$$\hat{\rho} = \frac{1}{2}\left(1 + \frac{1}{L}\sum_{i=1}^{L}\sigma_i^z\right) . \tag{3.22}$$

Let E_ϵ the second-lowest eigenvalue whose eigenstate $|\epsilon\rangle$ is *even* under cyclic translation. In the thermodynamic limit, these two even eigenvalues E_0 and E_ϵ cross with each other at a first-order transition point. Applying degenerate perturbation theory to the $L \to \infty$ limit, one finds [57] that the densities which correspond to the high- and low-density phases are given by the solutions of

$$\begin{vmatrix} \langle 0|\hat{\rho}|0\rangle - \rho & \langle 0|\hat{\rho}|\epsilon\rangle \\ \langle \epsilon|\hat{\rho}|0\rangle & \langle \epsilon|\hat{\rho}|\epsilon\rangle - \rho \end{vmatrix} = 0 . \tag{3.23}$$

The largest odd eigenvalues also become degenerate with the largest even ones. However, they do *not* affect Eq. (3.23), because the off-diagonal elements always vanish due to the symmetry.

Thus, the densities at a transition point are given by

$$\rho_\pm = \rho_c \pm \frac{\Delta\rho}{2} \tag{3.24}$$

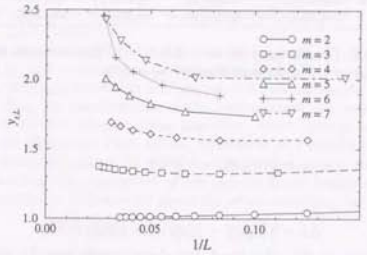

FIGURE 3.1. Effective thermal exponent $y_{t,L}$ for $m = 2, \cdots, 7$.

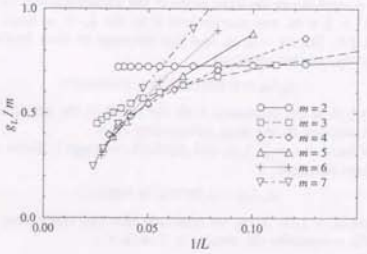

FIGURE 3.2. Effective scaled gap g_L for $m = 2, \cdots, 7$.

m	ρ_c/ρ_0		$\Delta\rho/\rho_0$	
	L	$L+m$	L	$L+m$
2	0.6891672(7)	0.689168(1)	0.00002(3)	0.0000(1)
3	0.7871(3)	0.7870(5)	0.010(1)	0.01(1)
4	0.825(2)	0.825(2)	0.036(3)	0.05(2)
5	0.867(4)	0.867(6)	0.056(6)	0.07(2)
6	0.902(6)	0.899(9)	0.076(7)	0.09(2)
7	0.925(7)	0.927(9)	0.087(6)	0.11(2)

TABLE 3.3. Density gaps for $m = 2, 3, \cdots, 7$. The densities herein are normalized by the maximum density: $\rho_0 = 1/m$.

with

$$\rho_c = \frac{1}{2}(\langle 0|\hat{\rho}|0\rangle + \langle \epsilon|\hat{\rho}|\epsilon\rangle) \tag{3.25}$$

and

$$\Delta\rho = [(\langle 0|\hat{\rho}|0\rangle - \langle \epsilon|\hat{\rho}|\epsilon\rangle)^2 + 4\langle 0|\hat{\rho}|\epsilon\rangle^2]^{1/2}. \tag{3.26}$$

For a finite system, on the other hand, the above density gap $\Delta\rho$ always has a finite value. For a second-order transition, it vanishes as $L^{-(1-\alpha)/\nu}$, while it remains finite for a first-order transition. This scheme has been applied for the p-state Potts model [58] and interacting hard squares [59] and it has been confirmed that it reproduces the exactly known results for the density gap or latent heat.

We evaluate ρ_c and $\Delta\rho$ at the fixed point of the phenomenological renormalization, μ_L^*, for L and $L' = L + m$, and extrapolate it to the $L \to \infty$ limit. The results are listed in TABLE 3.3. For $m = 2$, ρ_c and $\Delta\rho$ converge to their limits as $O(L^{-2})$ and $O(L^{-1})$, respectively, and we obtained

$$\rho_\pm/\rho_0 = 0.6891672(7) \pm 0.00001(2) \tag{3.27}$$

with $\rho_0 = 1/2$, which is the consistent with the result in the previous section, that is, a second-order transition in the Ising universality class.

On the other hand, for $m \geq 3$, ρ_c and $\Delta\rho$ both converge to finite values as $O(L^{-1})$. Especially, we have obtained

$$\rho_\pm/\rho_0 = 0.7871(3) \pm 0.005(1) \tag{3.28}$$

for $m = 3$, where $\rho_0 = 1/3$. Thus, we conclude that the transitions are of first order for all $m \geq 3$. We summarize our results in TABLE 3.3.

3.5. Summary and Discussion

In the present chapter, the phase transition of the quantum hard-rod system (3.1) has been studied. The model exhibits a solid–fluid phase transition, where the ordered phase has an m-fold degenerated antiferromagnetic-like order. For $m = 2, 3, \cdots, 7$ we performed exact diagonalization up to quite large system sizes ($L = 30 - 42$). For

the $m = 2$ model, we reconfirmed that the transition is of second order and that it belongs to the same universality class as the Ising model, which is consistent with the two-fold degeneracy of the ordered state, and with the symmetry of the order parameter. We also evaluated the critical point parameters ($\mu_c = 0.6550966(1)$ and $\rho_c/\rho_0 = 0.6891672(7)$) more accurately than the previous estimates [75]. For $m \geq 3$, we concluded the transition is of first order owing to the quick decay of the scaled gap and to the divergence of the thermal exponent. We also estimated the density gap directly and concluded finite density gaps for $m \geq 3$. Especially, for $m = 3$, we estimated the density gap as $\Delta\rho = 0.010(1)$.

The present quantum hard-rod model is a special limit of the multispin-coupling Ising model (3.2) with transverse and longitudinal fields. For $m = 2$, along the whole transition line, the phase transition is of second order and shows the Ising universality, as is expected from the consideration of the ordered-state degeneracy. On the other hand, for $m = 3$, the second-order phase transition, which belongs to the same universality class as the three-state Potts model, terminates at a multicritical point h_M, and the first-order transition occurs for $-3 \leq h_\ell < h_M$, where a naive classification on the universality, based on the degeneracy of the ordered state, breaks down. Finally, for $m \geq 4$, the transition is of first order along the whole transition line.

CHAPTER 4

Alder Transition of Hard Disks and Spheres in Continuous Space

4.1. Introduction

In the present chapter we change our subject to the problem of studying hard particles in the continuous space. An analytic equation of state of a hard-core system in the continuous space plays an important role as a reference system in perturbation theory [88] and other approximate theories for fluid systems. On the other hand, the hard-core system itself also has aroused a great deal of interest. In 1962 the existence of the solid–fluid phase transition of hard disks, so called the *Alder transition*, was indicated by the molecular-dynamics method [7], in spite that the system has only repulsive interaction. Since then, this system has been studied numerically and also analytically. (For reviews, see [89–91].)

One of the most successful methods to investigate the solid–fluid phase transition in hard-core systems is the molecular-dynamics method [7, 92, 93]. A plateau appears in the state diagram indicates a first-order phase transition, and their estimates of thermodynamic quantities coincide quite well with each other. Monte Carlo simulations have also been performed on this system and predicted a first-order transition [94–96].

In spite of the success in numerical simulations, theoretical understanding of the mechanism of the transition is by no means satisfactory. One of general theoretical approaches to this problem is based on the closed-form integral equations (the Born-Green equation [97], the Percus-Yevick equation [98], the hyper-netted chain equation [99], the Kirkwood equation [100–102], etc.) Especially, the Percus-Yevick equation for hard spheres has been solved analytically by Thiele [103] and by Wertheim [104, 105]. However, none of them can predict phase transitions.

There is another theoretical approach based on the virial expansion. It is the well-known Carnahan-Starling equation [106], and generalizations of this equation have also been proposed [107]. However, the physical meaning in their procedure is not so clear.

Recently, Hu and Suzuki [108] proposed a new intuitive argument by treating kinetics of particles using statistical mechanics. They derived an effective attraction between

particles by taking the *shadow effect* into account. They predicted a localization–delocalization transition, which may be related to the solid–fluid phase transition, only in two dimensions but not in three dimensions.

A theoretical equation of state for the hard-core system is expected to have the following form:

$$\frac{P}{kT\rho} = \frac{1}{(1-\rho/\rho_c)^{\lambda}}\{1+O(\rho)\}. \tag{4.1}$$

In the present chapter, we assume the above form of the singularity in the equation of state of the hard-core system and estimate the singular point ρ_c and the non-trivial exponent λ in two and three dimensions by means of the virial series expansion, namely, low-density expansion. In the low-density limit, the system is in the fluid (disordered) phase. Therefore, Eq. (4.1) with y_c and λ obtained through the virial expansion should describe the fluid branch.

If there were no phase transitions, the system may have only one singular point at the close-packing density ρ_{cp} and the state described by Eq. (4.1) is always stable for $0 \le \rho < \rho_{cp}$. Thus, $\rho_c = \rho_{cp}$. On the contrary, if the system were to exhibit a solid–fluid phase transition of first order, there exists another branch (solid branch), which has a singular point at ρ_{cp}, and it is not necessary for ρ_c in Eq. (4.1) to equal ρ_{cp} any more.

In the next section, the virial expansion and coefficients of the hard-core system are briefly reviewed, and the Padé approximant for the virial expansion is constructed. In section 4.3, we analyze the canonical series of the Padé approximants by means of the coherent-anomaly method [109–111] and conclude that the singular point ρ_c is equal to the density at the packing fraction of unity and the exponent λ is equal to the dimensionality of the space [112]. In the final section of the present chapter, we discuss physical meaning and interpretation of our results and make a comparison with other methods.

4.2. Virial Expansion and Padé Approximant

The virial coefficients $\{B_i\}$ are defined as the following coefficients in the expansion of the pressure in powers of the density:

$$\frac{P}{kT} = B_1 y + B_2 y^2 + B_3 y^3 + B_4 y^4 + \cdots, \tag{4.2}$$

where P is the pressure, T the temperature, k the Boltzmann constant, and the variable y is the density. Hereafter, we use the dimensionless density defined as follows:

$$y = \frac{N}{V} S_d, \tag{4.3}$$

where N is the number of particles, V is the volume of the system, and S_d is the volume of a particle of diameter σ in d dimensions.* ($S_d = \sigma$, $\pi\sigma^2/4$, and $\pi\sigma^3/6$ for $d = 1$, 2, and 3, respectively.) The density defined above is called the *packing fraction*.

*For arbitrary dimensionality, $S_d = \pi^{d/2}\sigma^d/2^{d-1}d\Gamma(d/2)$. On the other hand, the close-packing density is not trivial at all and has not been solved yet in higher dimensions. It remains as a challenging problem in connection with the application to digital communications. (For reviews, see [113])

The reduced pressure P/kT is also normalized so that the first virial coefficient B_1 in Eq. (4.2) may become unity. In terms of the packing fraction, the close-packing density is given by

$$y_{cp} = \begin{cases} 1 & \text{in one dimension,} \\ \sqrt{3}\pi/6 = 0.907 & \text{in two dimensions,} \\ \sqrt{2}\pi/6 = 0.740 & \text{in three dimensions.} \end{cases} \tag{4.4}$$

The density at the packing fraction of unity, $y = 1$, corresponds to the density at which all the space is filled and apparently cannot be realized in dimensions higher than one.

As mentioned in chapter 1, the reduced pressure P/kT of the pure hard-core system does *not* depend on the temperature; it depends only on the density. Therefore, the virial coefficients become temperature-independent constants. In one dimension, the equation of state of hard rods is given by

$$\frac{P}{kT} = \frac{y}{1-y}, \tag{4.5}$$

which is well known as Tonks' exact solution [114], and all the virial coefficients become unity, consequently. In two and three dimensions, the virial coefficients only up to the fourth order are known exactly by explicit integration [114–120], while higher coefficients are calculated approximately up to the eighth order by numerical evaluation of the cluster integrals [121–131]:

$$\begin{aligned} &B_2 = 2, \\ &B_3 = \frac{16}{3} - \frac{4\sqrt{3}}{\pi} = 3.1280177\cdots, \\ &B_4 = 16 - \frac{36\sqrt{3}}{\pi} + \frac{80}{\pi^2} = 4.2578544\cdots, \\ &B_5 = 5.3368966(6), \\ &B_6 = 6.3626(3), \\ &B_7 = 7.351(4), \text{ and} \\ &B_8 = 8.34(1) \qquad \text{in two dimensions,} \end{aligned} \tag{4.6}$$

and

$$\begin{aligned} &B_2 = 4, \\ &B_3 = 10, \\ &B_4 = -\frac{712}{35} + \frac{219\sqrt{2}}{35\pi} + \frac{4131}{35\pi}\arccos\left(\frac{1}{\sqrt{3}}\right) = 18.36477\cdots, \\ &B_5 = 28.2245(3), \\ &B_6 = 39.74(6), \\ &B_7 = 53.5(3), \text{ and} \\ &B_8 = 71(2) \qquad \text{in three dimensions.} \end{aligned} \tag{4.7}$$

$[L,M]$	[0,1]	[1,1]	[2,1]	[3,1]	[4,1]	[5,1]	[6,1]
p_1		0.4360	0.6388	0.7466	0.8078(1)	0.8447(8)	0.866(2)
p_2			0.4056	0.6212	0.7436(1)	0.817(2)	0.859(4)
p_3				0.3371	0.5287(2)	0.644(2)	0.710(7)
p_4					0.2608(3)	0.418(3)	0.573(9)
p_5						0.197(4)	0.31(1)
p_6							0.13(2)
y_c	0.5	0.6394	0.7346	0.7978	0.8388	0.8655(6)	0.882(2)
$\bar{Z}$	1	1.2788	1.6882	2.1622	2.6419(5)	3.09(1)	3.45(4)
p_1		1.5	2.1635	2.4631	2.59(2)	2.653(9)	2.68(4)
p_2			2.6541	3.8525(1)	4.37(8)	4.61(4)	4.7(2)
p_3				2.9960(1)	4.29(2)	4.89(9)	5.1(4)
p_4					2.37(4)	3.5(2)	3.9(7)
p_5						1.7(3)	2(1)
p_6							1(2)
y_c	0.25	0.4	0.5445	0.6507	0.710(1)	0.742(5)	0.76(2)
$\bar{Z}$	1	1.6	2.9650	5.0590(1)	7.18(4)	9.0(3)	10(2)

TABLE 4.1. Coefficients of the Padé approximants in two (above) and three (below) dimensions. The approximate singular point and the critical coefficient are also listed in. We have omitted the coefficients p_0, r_0, and r_1, because $p_0 = r_0 = 1$ and $r_1 = -y_c^{-1}$, obviously.

Note that all of these coefficients are positive at least up to the present order.[†] If we consider a polynomial obtained by truncating the virial expansion Eq. (4.2) at first N terms ($N \leq 8$), it increases monotonically as the density does. There is no singular point in this finite-order polynomial. A singularity appears when we sum up all the terms up to infinite order by means of the Padé approximant or other re-summation techniques.

A Padé approximant $Q^{[L,M]}(x)$ to a function $F(x)$ is defined as a ratio of two polynomials:

$$Q^{[L,M]}(x) = \frac{P(x)}{R(x)} = \frac{p_0 + p_1 x + p_2 x^2 + \cdots + p_L x^L}{r_0 + r_1 x + r_2 x^2 + \cdots + r_M x^M}. \tag{4.8}$$

The coefficient r_0 can be taken as unity without loss of generality. The other coefficients $\{p_i\}$ and $\{r_i\}$ are chosen so that the expansion of $Q^{[L,M]}(x)$ in powers of x may agree with the expansion of $F(x)$ for the first $(L+M+1)$ terms.

The Padé approximants for the compressibility factor $Z(y) \equiv P/kTy$ are constructed [112] for $[0,1] \sim [6,1]$. The coefficients in these approximants are listed in TABLE 4.1. Each of these approximants has a simple pole at a finite density y_c, and near this pole the behavior of the approximate compressibility factor can be represented

[†]However, in higher dimensions, the fourth virial coefficient can be negative. The critical dimension has been estimated as ~ 7.8 by Luban and Baram [132].

as the following skeletonized form:

$$Z(y) = \frac{P}{kTy} \simeq \frac{\bar{Z}(y_c)}{1 - y/y_c}. \tag{4.9}$$

The residue of the divergence, $\bar{Z}$, is called the *critical coefficient*.

4.3. Coherent-Anomaly Method

Although the approximate singular point y_c of the Padé approximant approaches the true singular point y_c^* by improving the degree of approximation, the singularity at the critical point remains classical. On the other hand, the critical coefficient $\bar{Z}$ tends to diverge systematically as seen in TABLE 4.1. This is due to the discrepancy between the classical singularities of the Padé approximants and the expected singularity:

$$Z(y) \sim \frac{1}{(1 - y/y_c^*)^\lambda}. \tag{4.10}$$

with the non-trivial exponent λ. According to the coherent-anomaly method [109–111], the critical coefficient is presumed to exhibit the following anomalous behavior:

$$\bar{Z}(y_c) \simeq \frac{f}{(y_c^* - y_c)^\psi} \tag{4.11}$$

as $y_c \to y_c^*$. This behavior is referred as the *coherent anomaly*. The exponent of the true singularity is then evaluated through the following coherent-anomaly relation:

$$\lambda = \psi + 1. \tag{4.12}$$

We can thus obtain the true non-trivial exponent λ by estimating the fitting parameters f, y_c^*, and ψ in Eq. (4.11).

The Padé approximants for the hard-core systems are shown to exhibit clear coherent anomalies [112] (TABLE 4.1). In two dimensions, by the least-squares fitting for $[L,M] = [2,1] \sim [6,1]$, we obtained $y_c^* = 1.02$ and $\lambda = 1.98$ (or $y_c^* = 1.01$ and $\lambda = 1.95$ for $[L,M] = [1,1] \sim [6,1]$). Note that the estimate for y_c^* is very close to unity. In three dimensions, on the other hand, $y_c^* = 1.06$ was obtained by the least-squares fitting for $[L,M] = [2,1] \sim [6,1]$. If we assume that the true singular point is at the packing fraction of unity as is in the two-dimensional case, we obtain $\lambda = 2.94$ for $[L,M] = [2,1] \sim [6,1]$ (or $\lambda = 3.02$ for $[L,M] = [1,1] \sim [6,1]$.) The plots for these fittings are shown in FIGURES 4.1 and 4.2.

4.4. Discussions

In both cases the estimated singular point y_c^* is close to the packing fraction of unity and the exponent λ is also close to the dimensionality of the space. Thus, we propose the following unified form [112]:

$$Z(y) \sim \frac{1}{(1-y)^d} \tag{4.13}$$

for d-dimensional hard-core systems.

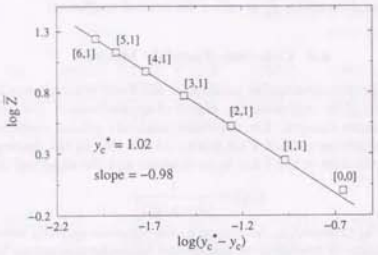

FIGURE 4.1. The CAM plot of the data in two dimensions. The solid line is obtained by means of least-squares fitting for the Padé approximants $[2,1] \sim [6,1]$. The slope of this line corresponds to $(1 - \lambda)$ according to the coherent-anomaly method. The error of estimate does not exceed the symbol size.

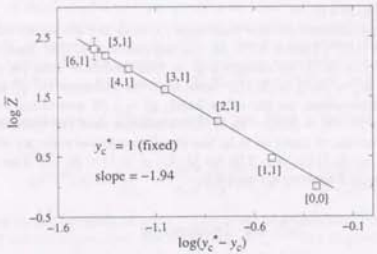

FIGURE 4.2. The CAM plot of the data in three dimensions. The solid line is obtained by means of least-squares fitting for the Padé approximants $[2,1] \sim [6,1]$. The singular point y_c^* is fixed to be unity. The error of estimate does not exceed the symbol size except for $[6,1]$.

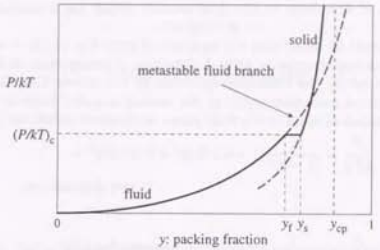

FIGURE 4.3. A schematic state diagram of the hard-core system in dimensions higher than one. The stable state is denoted by the thick solid line. At the critical reduced pressure $(P/kT)_c$, the first-order phase transition occurs and the density jumps from y_f to y_s. In the solid phase, the reduced pressure diverges at the close-packing density y_{cp}. The metastable fluid branch (long-dashed line), on the other hand, seems to diverge at the packing fraction of unity ($y = 1$) [112]. In two dimensions, for example, $y_f = 0.711(2)$ and $y_s = 0.726(3)$ by the molecular-dynamics simulation [93], and $y_{cp} = 0.907$.

The density at the packing fraction of unity, $y = 1$, is an unphysical pole, because it is greater than the close-packing density y_{cp} (see Eq. (4.4)). On the other hand, the existence of the unphysical pole at the packing fraction of unity is consistent with the well-known Thiele and Wertheim solution of the Percus-Yevick equation [98, 103–105] and with the analyses of computer-simulation data by means of the Padé approximant [107].

Our conjecture Eq. (4.13) is also supported by the existence of the universal fluid branch when one introduces bi- or poly-dispersities into particle-radii distributions. The molecular-dynamics simulations [133] have shown that the fluid branch is *not* so sensitive to the bi- and poly-dispersities, although the solid branch is extremely affected by the change of the close-packing density. This fact implies that the particles in the fluid phase are excluded by the volume of particles themselves.

Moreover, Eq. (4.13) is consistent with the rigorous result in one dimension, the nonexistence of the transition. In one dimension, the volume of a hard particle, namely, the length of a hard rod, is identical to the close-packing volume. Hence, Eq. (4.13) also holds exactly in one dimension, as is seen from Tonks' exact solution, Eq. (4.5).

Thus, we conclude that the hard particles in the fluid phase are excluded effectively not by the close-packing volume but by the volume of particles themselves [112]. In dimensions higher than one, it is impossible for the system to attain the density

at the packing fraction of unity. Therefore, because of the discrepancy between the density at the packing fraction of unity and the close-packing density, there occurs a phase transition of first order to the solid branch, which has a singular point at y_{cp} (FIGURE 4.3).

Finally, it should be noted that the equation of state Eq. (4.13) is valid only when describing the leading singularity at high densities. Consequently, it fails to predict the results obtained by the molecular-dynamics or the Monte Carlo simulations. If we take into account correction terms to the leading singular behavior, however, the quantitative equation of state in the fluid phase is obtained as follows [112]:

$$\frac{P}{kTy} = \frac{1}{(1-y)^2}(1 + 0.1280y^2 + 0.00182y^3 + \cdots) \qquad \text{in two dimensions,} \tag{4.14}$$

and

$$\frac{P}{kTy} = \frac{1}{(1-y)^3}(1 + y + y^2 - 0.6352y^3 + \cdots) \qquad \text{in three dimensions.} \tag{4.15}$$

Here, the coefficients of the correction terms are chosen so that the expansion of *r.h.s.* may reproduce the correct virial coefficients.

CHAPTER 5

Concluding Remarks

In the present thesis, we have investigated several systems with hard-core potential in conjunction with the first-order solid–fluid phase transitions.

In chapter 2, we have discussed the two-dimensional classical lattice gases with the nearest-neighbor exclusion and the next-nearest neighbor interaction, by means of the transfer-matrix method, the phenomenological renormalization, and the conformal invariance. To calculate the transfer matrix of much larger systems than the previous works, we have proposed a new method based on the sparse-matrix factorization and the dimensional reduction of the transfer matrix. This method has been discussed in detail in appendices. By using our improved method, we obtained some new results and found the phase diagram of the hard-core lattice gases on the triangular and square lattices. Especially, we concluded that the second-order transitions of the hard-core lattice gases can be quite generally classified into the corresponding Potts models in terms of the degeneracy of the ordered state.

In chapter 3, the ground-state phase transition of the one-dimensional quantum hard-core lattice gas (quantum hard rods) has been investigated. We have performed the diagonalization of the eigenvalue matrix for $2 \leq m \leq 7$, where m corresponds to the length of a hard rod. The maximum number of lattice sites is $L = 49$, which is quite larger than the previous works. In the case of $m = 2$, the phase transition is of second order and belongs to the same universality class as the Ising model. On the other hand, for $m \geq 3$, we confirmed that the transition is of first order. We have also estimated the density gap associated with the first-order transition accurately and concluded it is finite for $m \geq 3$ and becomes larger as the m increases.

In chapter 4, we have studied the equation of state in the fluid phase of the hard-core system in the continuous space by means of the virial expansion. By using the Padé approximant and the coherent-anomaly method, the singularity of the equation of state of the fluid branch:

$$\frac{P}{kT\rho} = \frac{1}{(1-\rho/\rho_c)^\lambda}\{1 + O(\rho)\}$$

has been investigated. As a result, we have concluded that the singular point ρ_c is equal to the density at the packing fraction of unity and the exponent λ is also equal

to the dimensionality of the space. The density at the packing fraction of unity is an unphysical pole, because it is greater than the close-packing density in dimensions higher than one. This result therefore implies the existence of another branch, which corresponds to the solid phase, and the solid–fluid phase transition of first order (the Alder transition).

We have thus obtained several new results and aspects in the phase transitions of the systems with hard-core potential. On the other hand, however, understanding of the essential mechanism in the solid–fluid phase transition still remains unsatisfactory. In this respect, further extensive theoretical and numerical investigations are to be desired.

APPENDIX A

Sparse-Matrix Factorization for Hard-Core Lattice Gas

In the present appendix, we discuss in detail a new method to treat large-scale transfer matrices of the hard-core lattice gases in numerical calculations. As an example, hereafter we consider a nearest-neighbor lattice-gas Hamiltonian on the square lattice:

$$-\beta\mathcal{H} = U\sum_i n_i + W\sum_{\langle i,j\rangle} n_i n_j\,, \tag{A.1}$$

where U is the reduced chemical potential, W the reduced nearest-neighbor interaction (attractive for $W > 0$ and repulsive for $W < 0$), and n_i is the occupation number of the ith site. The lattice has an infinite length in one direction (referred to as the *transfer* direction) and the periodic boundary conditions are applied in the other direction (the *length* direction).

A transfer matrix of this Hamiltonian can be defined as follows:

$$\mathbb{T}(\tau|\sigma) = \exp\left[\sum_{i=1}^{N}\left\{\frac{W}{2}(2\,\tau_i\sigma_i + \tau_i\tau_{i+1} + \sigma_i\sigma_{i+1}) + \frac{U}{2}(\tau_i + \sigma_i)\right\}\right]\,, \tag{A.2}$$

where the transfer direction is selected as 'row-to-row' (FIGURE 2.5 (b) on p. 12), and the unit slices are then chosen to be rows. The configurations $\sigma = (\sigma_1, \sigma_2, \cdots, \sigma_N)$ and $\tau = (\tau_1, \tau_2, \cdots, \tau_N)$ denote those on two neighboring rows.

Sparse-Matrix Factorization. The transfer matrix (A.2) is a dense matrix; its elements vanish only if there is infinite repulsion ($W \to -\infty$). However, use of this matrix in this form in numerical applications is highly inefficient. For example, multiplication of a trial vector by the transfer matrix requires on the order of 2^{2N} elementary arithmetic operations. In addition, it requires the memory storage of the same order to store the matrix elements. However, by using sparse matrices, the number of operations and the use of the memory storage can be extremely reduced [14].

For example, the transfer matrix (A.2) can be factorized into

$$\mathbb{T} = \mathbb{D}^{1/2}\cdot\mathbb{M}_N\cdot\mathbb{M}_{N-1}\cdots\mathbb{M}_1\cdot\mathbb{D}^{1/2}\,, \tag{A.3}$$

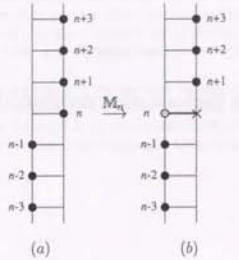

FIGURE A.1. The step-transfer matrix $\mathbb{M}_n$ (Eq. (A.5)), which adds a horizontal bond (thick line). That is, it transfers the nth site to the next row.

where the *in-slice* matrix $\mathbb{D}$ and the *step-transfer* matrices $\mathbb{M}_n$ are defined as follows:*

$$\mathbb{D}(\tau|\sigma) = \left(\prod_{i=1}^{N} \delta_{\tau_i,\sigma_i}\right) \exp\left[\sum_{i=1}^{N} (W\sigma_i\sigma_{i+1} + U\sigma_i)\right] , \tag{A.4}$$

and

$$\mathbb{M}_n(\tau|\sigma) = \left(\prod_{i\neq n} \delta_{\tau_i,\sigma_i}\right) \exp\left[W\tau_n\sigma_n\right] . \tag{A.5}$$

The sparseness of these matrices is manifested by the Kronecker delta functions. Indeed, $\mathbb{D}$ is a diagonal matrix and $\mathbb{M}_n$ is a matrix with only 2^{N+1} non-zero elements. The step-transfer matrix $\mathbb{M}_n$ adds one horizontal bond, which connect between τ_n and σ_n. In other words, it transfers the nth site on a unit slice to the adjacent site on the next row (FIGURE A.1), while the other sites are not affected at all. After N steps (via $(N-1)$ intermediate states), all the sites have been transferred to the next unit slice. Note that these intermediate states, or slices, are *not* geometrically identical to the original unit slice.

In terms of the factorized matrix (A.3), the number of operations and the use of the memory storage are reduced to roughly $N2^N$ and 2^N, respectively. This factorization technique also can be applied to the case of other boundary conditions, or further-nearest-neighbor interactions [24, 134, 135].

Dimensional Reduction. On the other hand, if there are infinite near-neighbor repulsions, another scheme for reducing the number of operations and the use of the memory storage is possible. In the presence of the near-neighbor exclusions, the number of possible configurations on a unit slice is highly reduced. For example, that of the transfer matrix (A.2) with $W \to -\infty$ is only λ^N for $N \gg 1$, rather than 2^N ($\lambda = 1.61803\cdots$ in this case. See appendix B). If we restrict ourselves in this highly reduced configuration space (referred to as $\psi_2^{(p)}$ in appendix B), the transfer matrix (A.2) can be simplified to the following form:

$$\mathbb{T}(\tau|\sigma) = \prod_{i=1}^{N} \left\{ (1 - \tau_i\sigma_i) \exp\left[\frac{U}{2}(\tau_i + \sigma_i)\right] \right\} , \tag{A.6}$$

where σ and τ denote configurations in the restricted space of dimension $O(\lambda^N)$. Note that the exclusions *within* the unit slices ($\sum \tau_i\tau_{i+1}$ and $\sum \sigma_i\sigma_{i+1}$ in Eq. (A.2)) have been already taken into account by considering the restricted configuration space. The number of operations and the use of the memory storage associated with multiplication by this matrix are reduced to the order of λ^{2N}. This technique has been applied frequently to the hard-core lattice gases [43, 60, 136].

Sparse-Matrix Factorization for Hard-Core Lattice Gas. The dimensional-reduction technique above mentioned is also quite efficient as the sparse-matrix factorization. For example, the transfer matrix (A.2) with $W = -\infty$ is tractable up to $N = 19$ and 24 on a computer with the main memory of 1 Gbytes by using the dimensional reduction and the sparse-matrix factorization, respectively, while if one use the original *dense* transfer matrix, the maximum size is limited only to $N = 13$.

However, in a usual manner, these useful methods are *not* compatible with each other at all. In the sparse-matrix-factorization scheme, a transfer process from a unit slice to the next one is divided into N steps. In each step, only one site is transferred to the next unit slice (FIGURE A.1). At intermediate stages, the shape of the slice is not identical to that of the original unit slice. In the case of FIGURE A.1 (a), for example, the nth site is not a nearest neighbor of the $(n-1)$th site. Therefore, these two sites can be occupied at the same time; apparently such a configuration is not contained in our restricted space. Similar situations can occur everywhere in the intermediate steps. Thus, the dimensional reduction does not work in this case.

This difficulty can be overcome by using a slightly modified step-transfer process. In our modified process, a site is transferred to the diagonal direction instead of to its adjacent site (FIGURE A.2). During this process the ith site ($i = 1, 2, \cdots, N-1$) always stays as a nearest neighbor of the $(i+1)$th site. As is seen in FIGURE A.2, the Nth site is *not* a nearest neighbor of the 1st site in the intermediate steps. Moreover, we have to introduce an additional $(N+1)$th site in order that all the contributions of the interaction are correctly taken into account. Thus, in our modified transfer process, the dimension of the matrix should be slightly extended to $2 \times d_2^{(o)}(N)$.

Thus, there are $2 \times d_2^{(o)}(N)$ possible states of $(N+1)$ sites in the intermediate states. However, it should be noted that the matrix is decomposed into two blocks corresponding to different values of the $(N+1)$th site. So the number of intermediate results to be stored simultaneously on the memory storage is only $d_2^{(o)}(N)$.

*In practice, the in-slice matrix $\mathbb{D}$ is further decomposed into simpler matrices, that is, $\mathbb{D} = \prod_{n=1}^{N} \mathbb{D}_n$, where $\mathbb{D}_n(\tau|\sigma) = (\prod_{i=1}^{N} \delta_{\tau_i,\sigma_i}) \exp[W\sigma_n\sigma_{n+1} + U\sigma_n]$.

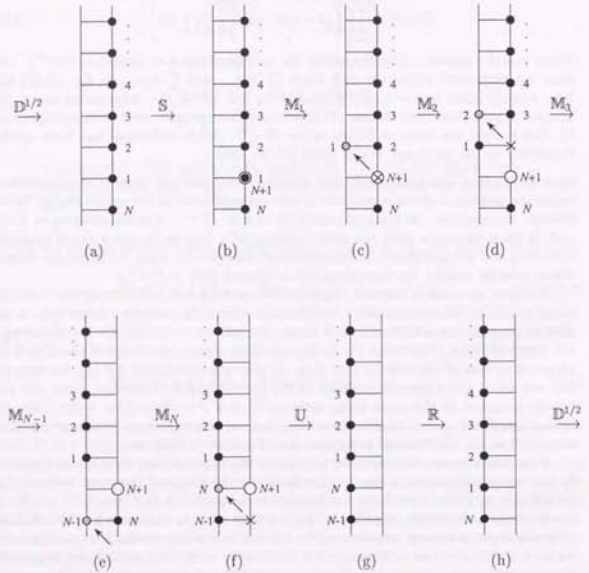

FIGURE A.2. Modified transfer process for hard squares. For definitions of the matrices, see the text.

method	time	memory	$N_{\max}$
original dense matrix	2^{2N}	2^{2N}	13
dimensional reduction	λ^{2N}	λ^{2N}	19
sparse-matrix factorization	$N2^N$	2^N	24
present method	$N\lambda^N$	λ^N	**35**

TABLE A.1. Maximum system size of the transfer matrix for hard squares by the various methods.

By using the above step-transfer process, the transfer matrix (A.2) can be explicitly decomposed into the following sparse matrices:

$$\mathbf{T} = \mathbb{D}^{1/2} \cdot \mathbb{R} \cdot \mathbf{U} \cdot \mathbb{M}_N \cdot \mathbb{M}_{N-1} \cdots \mathbb{M}_1 \cdot \mathbf{S}_1 \cdot \mathbb{D}^{1/2} , \tag{A.7}$$

with

$$\mathbb{D}(\tau|\sigma) = \left(\prod_{i=1}^{N} \delta_{\tau_i,\sigma_i} \right) \{1 - \sigma_1\sigma_N\} \exp\left[U \sum_{i=1}^{N} \sigma_i \right] , \tag{A.8}$$

$$\mathbf{S}_1(\bar{\tau}|\sigma) = \left(\prod_{i=1}^{N} \delta_{\tau_i,\sigma_i} \right) \delta_{\tau_{N+1},\sigma_1} , \tag{A.9}$$

$$\mathbb{M}_n(\bar{\tau}|\bar{\sigma}) = \left(\prod_{i\neq n} \delta_{\tau_i,\sigma_i} \right) , \tag{A.10}$$

$$\mathbf{U}(\tau|\bar{\sigma}) = \left(\prod_{i=1}^{N} \delta_{\tau_i,\sigma_i} \right) \{1 - \sigma_N\sigma_{N+1}\} , \tag{A.11}$$

$$\mathbb{R}(\tau|\sigma) = \left(\prod_{i=1}^{N-1} \delta_{\tau_{i+1},\sigma_i} \right) \delta_{\tau_1,\sigma_N} , \tag{A.12}$$

where $\bar{\sigma}$ and $\bar{\tau}$ denote a configuration in the extended space of $(N+1)$ sites. The *in-slice* matrix $\mathbb{D}$ counts the contribution *within* a unit slice. The *extension matrix* $\mathbf{S}$ extends the dimension of the configuration space by a factor 2 with $(N+1)$ sites. The *step-transfer matrix* $\mathbb{M}$, which is defined on the above extended space, transfers only one site to the diagonal direction. The *reduction matrix* $\mathbf{U}$ reduces the dimension of the configuration space extended by the extension matrix $\mathbf{S}$ to the original one. Finally, the *rotation matrix* $\mathbb{R}$ generates a cyclic translation by one site in a unit slice. Note that $\mathbf{S}$ and $\mathbf{U}$ are *not* square matrices. (FIGURE A.2)

For comparison, in TABLE A.1, we summarize the maximum system size tractable on a computer with memory storage of 1 Gbytes by using the methods discussed in this appendix. The efficiency of the present method is apparent.

The above sparse-matrix factorization in the restricted space can be also applied to the models on the triangular lattice and those with the further-nearest neighbor interaction. We present explicit expressions for these transfer matrices in appendix C.

APPENDIX B

Counting Possible States

In this appendix we consider the dimension of the transfer matrix for the hard-core lattice gas which appears in chapter 2. In the case of the ordinary Ising model, the dimension of the transfer matrix is given by 2^N, where N is the number of lattice sites involved in *a unit slice* of the transfer matrix. For the hard-core lattice gases, however, the number of possible states in a unit slice is highly reduced owing to the presence of the near-neighbor exclusion.

Let us consider an open chain of length N (FIGURE B.1 (a)). To each site a one-bit variable s_i $(i = 1, 2, \cdots, N)$ is assigned. Here $s_i = 1$ (0) means that the ith site is occupied (empty). The number of possible states is apparently 2^N, if there is no restriction. We call the space of these configurations as $\psi_1^{(o)}(N)$, and the number of states as $d_1^{(o)}(N)$. If there is an exclusion up to the $(m-1)$th-nearest neighbors, some of these configurations should be prohibited. We call the restricted space of the remaining possible states as $\psi_m^{(o)}(N)$ and its dimension as $d_m^{(o)}(N)$.

Similarly, on the *periodic* chain of length N, we also define the configuration space $\psi_m^{(p)}(N)$ and its dimension $d_m^{(p)}(N)$. Obviously, these configuration spaces and their dimensions satisfy the following relations:

$$
\begin{aligned}
&\psi_1^{(p)}(N) = \psi_1^{(o)}(N)\,, \\
&\psi_m^{(p)}(N) \subset \psi_m^{(o)}(N) \quad \text{for } m \geq 2, \\
&\psi_m^{(o)}(N) \subset \psi_{m-1}^{(o)}(N) \subset \cdots \subset \psi_1^{(o)}(N)\,, \\
&\psi_m^{(p)}(N) \subset \psi_{m-1}^{(p)}(N) \subset \cdots \subset \psi_1^{(p)}(N)\,, \\
&d_1^{(p)}(N) = d_1^{(o)}(N) = 2^N\,, \\
&d_m^{(p)}(N) < d_m^{(o)}(N) \quad \text{for } m \geq 2, \\
&d_m^{(p)}(N) < d_{m-1}^{(p)}(N) < \cdots < d_1^{(p)}(N) = 2^N\,, \\
&d_m^{(o)}(N) < d_{m-1}^{(o)}(N) < \cdots < d_1^{(o)}(N) = 2^N\,.
\end{aligned}
\tag{B.1}
$$

As shown below, the dimension of these spaces can be obtained in terms of a set of recursive formulas.

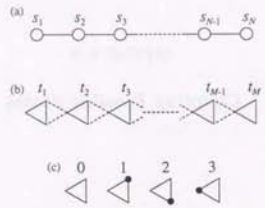

FIGURE B.1. Open chain (a), triangle chain (b), and four possible states on each triangle (c). Here, $M = N/3$.

Nearest-neighbor exclusion case. First we consider the case of $m = 2$. We define $n_0(N)$ and $n_1(N)$ as follows; $n_k(N)$ denotes the number of states, which satisfies $s_N = k$, in the configuration space $\psi_2^{(o)}(N)$. Clearly, $d_2^{(o)}(N) = n_0(N) + n_1(N)$. Suppose we add a new $(N+1)$th site. If $s_N = 1$, then $s_{N+1} = 1$ is not allowed. Thus, $n_0(N)$ and $n_1(N)$ satisfy the following recursive formulas:

$$\begin{pmatrix} n_0(N+1) \\ n_1(N+1) \end{pmatrix} = \begin{pmatrix} 1 & 1 \\ 1 & 0 \end{pmatrix} \begin{pmatrix} n_0(N) \\ n_1(N) \end{pmatrix}, \tag{B.2}$$

with

$$n_0(1) = n_1(1) = 1. \tag{B.3}$$

This recursive formulas can be easily solved to give

$$\begin{aligned} d_2^{(o)}(N) &= n_0(N) + n_1(N) \\ &= \frac{5+3\sqrt{3}}{10}\left(\frac{1+\sqrt{5}}{2}\right)^N + \frac{5-3\sqrt{3}}{10}\left(\frac{1-\sqrt{5}}{2}\right)^N . \end{aligned} \tag{B.4}$$

For large N, $d_2^{(o)}(N)$ behaves asymptotically as

$$\begin{aligned} d_2^{(o)}(N) &\simeq \frac{5+3\sqrt{3}}{10}\left(\frac{1+\sqrt{5}}{2}\right)^N \\ &= 1.17082 \times (1.61803)^N . \end{aligned} \tag{B.5}$$

m	λ_m	a_m
1	2	1
2	1.61803	1.17082
3	1.46557	1.31342
4	1.38028	1.43971
5	1.32472	1.55497
6	1.28520	1.66212
7	1.25542	1.76297

TABLE B.1. Constants in Eqs. (B.11) and (B.12).

In the case of the periodic chain, some states, where $s_1 = 1$ and $s_N = 1$, are prohibited owing to the periodicity. Therefore,

$$\begin{aligned} d_2^{(p)}(N) &= d_2^{(o)}(N) - d_2^{(o)}(N-4) \\ &= \left(\frac{1+\sqrt{5}}{2}\right)^N + \left(\frac{1-\sqrt{5}}{2}\right)^N \\ &\simeq (1.61803)^N \quad \text{for } N \gg 1. \end{aligned} \tag{B.6}$$

Further-nearest-neighbor exclusion case. The above procedure can be easily generalized for $m \geq 3$. The recursion relations for general m can be written in a matrix form as follows:

$$\begin{pmatrix} n_0(N+1) \\ n_1(N+1) \\ n_2(N+1) \\ \vdots \\ n_{m-1}(N+1) \end{pmatrix} = \begin{pmatrix} 1 & & & & 1 \\ 1 & 0 & & & \\ & 1 & 0 & & \\ & & \ddots & \ddots & \\ & & & 1 & 0 \end{pmatrix} \begin{pmatrix} n_0(N) \\ n_1(N) \\ n_2(N) \\ \vdots \\ n_{m-1}(N) \end{pmatrix} \tag{B.7}$$

with

$$n_k(1) = \begin{cases} 1 & \text{for } k = 0, 1 \\ 0 & \text{for } 2 \leq k \leq m-1, \end{cases} \tag{B.8}$$

where $n_0(N)$ denotes the number of possible states which satisfy $s_i = 0$ for $i = L-m+2, L-m+3, \cdots, L$, and $n_k(N)$ $(1 \leq k \leq m-1)$ is the number of possible states which satisfy $s_{L-m+k+1} = 1$ and $s_i = 0$ for $L-m+2 \leq i \leq L-m+k$ and $L-m+k+2 \leq i \leq L$.

The total number of possible states is given by

$$d_m^{(o)} = \sum_{k=1}^{m-1} n_k(N), \tag{B.9}$$

and

$$d_m^{(p)} = d_m^{(o)} - \sum_{k=1}^{m-1} k\, d_m^{(o)}(N-k-3), \tag{B.10}$$

	$N_{\max}$	
space	open	periodic
ψ_1	24	—
ψ_2	35	35
ψ_3	44	44
ψ_4	52	53
ψ_5	59	60
ψ_6	66	68
ψ_7	72	75
ϕ	36	—

TABLE B.2. $N_{\max}$ for ψ_m $(m = 1, 2, \cdots, 7)$ and ϕ.

for the open and periodic chains, respectively. It is too complicated to obtain an *analytic* closed-form expression for $m \geq 3$. Indeed, it is impossible for $m \geq 6$. The asymptotic behavior for $N \gg 1$ is given by

$$d_m^{(o)} \simeq a_m \lambda_m^N , \tag{B.11}$$

$$d_m^{(p)} \simeq \lambda_m^N , \tag{B.12}$$

where λ_m is the largest eigenvalue of the recursion matrix given in Eq. (B.7). It is obtained as the largest solution of the following characteristic equation,

$$\underbrace{\begin{vmatrix} 1-\lambda & & & & 1 \\ 1 & -\lambda & & & \\ & 1 & -\lambda & & \\ & & \ddots & \ddots & \\ & & & 1 & -\lambda \end{vmatrix}}_{m} = (1-\lambda) \underbrace{\begin{vmatrix} -\lambda & & & \\ 1 & -\lambda & & \\ & 1 & -\lambda & \\ & & \ddots & \ddots \\ & & & 1 & -\lambda \end{vmatrix}}_{m-1}$$

$$+ (-1)^{m+1} \underbrace{\begin{vmatrix} 1 & -\lambda & & & \\ & 1 & -\lambda & & \\ & & 1 & -\lambda & \\ & & & \ddots & \\ & & & & 1 \end{vmatrix}}_{m-1}$$

$$= (1-\lambda)(-\lambda)^{m-1} + (-1)^{m+1}$$

$$= (-1)^m \{\lambda^m - \lambda^{m-1} - 1\} = 0 , \tag{B.13}$$

and a_m is obtained from the elements of the eigenvector of the recursion matrix corresponding to the largest eigenvalue λ_m (TABLE B.1).

Triangular chain. When we consider a matrix which transfers in the direction parallel to a set of lattice edges on the triangular lattice (type (d) in TABLE 2.3 on p. 13), its unit slice is chosen as a triangular chain (FIGURE B.1 (b)). On each triangle, which contains three lattice sites, there are only four possible states (FIGURE B.1 (c)). If

we do not take the exclusion between the triangles into account, the dimension of the configuration space, referred to as $\phi(N)$, is simply given by

$$d_\phi(N) = 4^{N/3} = 1.58740^N . \tag{B.14}$$

Memory consideration. In terms of the matrix-diagonalization scheme such as the Lanczos method, we have only to store a few of *vectors* on the memory storage rather than the *transfer matrix* itself. Therefore, the maximum system size tractable on a computer with the main memory of M byte is estimated by

$$8 \times d_m(N_{\max}) \times n_v \simeq M . \tag{B.15}$$

Here n_v is the number of the vectors, and use of `Real*8` is assumed. Recent typical super computers have about 1 Gbyte ($\simeq 10^9$ byte) main memory. Thus, if we suppose $n_v = 5$, for example, we obtain

$$d_m(N_{\max}) \simeq 2.7 \times 10^7 . \tag{B.16}$$

In TABLE B.2, $N_{\max}$ are listed for the open and periodic chains and also for the triangle chain.

APPENDIX C

Explicit Expressions of Factorized Transfer Matrix

In this appendix we present explicit expressions of factorized transfer matrices used in chapter 2. The basic idea on the sparse-matrix factorization for the hard-core lattice gas has already been discussed in appendix A. Herein we consider eight different transfer matrices listed in TABLE 2.3 on p. 13.

Before we start discussing each transfer matrix, we review the sparse matrices which appear in the succeeding expressions:

- $\mathbf{D}$: the *in-slice matrix*, which adds bonds contained *in* a unit slice and also counts the contribution of the chemical potential.
- $\mathbf{S}_m$: the *extension matrix*, which extends the dimension of the configuration space by a factor 2^m. It can be written explicitly as

$$\mathbf{S}_m(\tilde{\tau}|\sigma) = \left(\prod_{i=1}^{N} \delta_{\tau_i,\sigma_i}\right) \prod_{k=1}^{m} \delta_{\tau_{N+k},\sigma_k}, \tag{C.1}$$

  where $\tilde{\tau} = (\tau_1, \cdots, \tau_N, \tau_{N+1}, \cdots, \tau_{N+m})$ denotes a configuration in the extended space.
- $\mathbf{M}_n$: the *step-transfer matrix*, which is defined on the extended space. It adds a few of bonds between neighboring unit slices.
- $\mathbf{U}$: the *reduction matrix*, which reduces the dimension of the configuration space extended by the extension matrix $\mathbf{S}$ to the original one.
- $\mathbf{R}$: the *rotation matrix*, which generates a cyclic translation by one site in a unit slice. It can be written explicitly by

$$\mathbf{R}(\tau|\sigma) = \left(\prod_{i=1}^{N-1} \delta_{\tau_{i+1},\sigma_i}\right) \delta_{\tau_1,\sigma_N}. \tag{C.2}$$

- $\mathbf{G}$: the *conjugation matrix*, which is defined so that $\mathbf{T}^{\dagger} = \mathbf{G} \cdot \mathbf{T} \cdot \mathbf{G}^{-1}$, where $\mathbf{T}^{\dagger}$ is a transpose of $\mathbf{T}$. If $\mathbf{v}$ is a *right* eigenvector of the transfer matrix $\mathbf{T}$, the corresponding *left* eigenvector $\mathbf{w}$ is given by $\mathbf{w} = \mathbf{G} \cdot \mathbf{v}$. Clearly, $\mathbf{G} = \mathbf{1}$ for symmetric matrices.

Note that $\mathbf{S}$ and $\mathbf{U}$ are *not* square matrices. The matrices $\mathbf{R}$ and $\mathbf{G}$ have only one non-vanishing element on each row and column. The *in-slice matrix* $\mathbf{D}$, which is a

diagonal matrix, is somewhat trivial. So we do not present its explicit expression (as an example, see Eq. (A.8) on p. 55).

TYPE (a). [lattice=triangle, direction=PD, interaction=(2+0), unit slice=(α), configuration space=$\psi_2^{(\alpha)}$, symmetric]*†

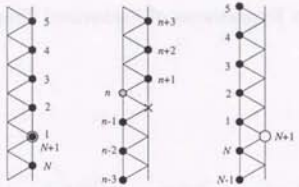

$$\mathbf{T} = \mathbf{D}^{1/2} \cdot \mathbf{U} \cdot \mathbf{M}_N \cdot \mathbf{M}_{N-1} \cdots \mathbf{M}_1 \cdot \mathbf{S}_1 \cdot \mathbf{D}^{1/2} \tag{C.3}$$

with

$$\mathbf{M}_n(\bar{\tau}|\bar{\sigma}) = \left(\prod_{i \neq n} \delta_{\tau_i,\sigma_i} \right) \{1 - \tau_n \sigma_n\} \tag{C.4}$$

$$\mathbf{U}(\tau|\bar{\sigma}) = \left(\prod_{i=1}^{N} \delta_{\tau_i,\sigma_i} \right) \{1 - \sigma_N \sigma_{N+1}\} . \tag{C.5}$$

Note that the matrix $\mathbf{T}$ is *not* symmetric. However, $\mathbb{T} = \mathbb{R} \cdot \mathbb{T}^2$ becomes symmetric.

TYPE (b). [lattice=square, direction=RR, interaction=(2+0), unit slice=(α), configuration space=$\psi_2^{(\alpha)}$, symmetric]

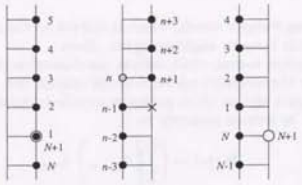

$$\mathbf{T} = \mathbf{D}^{1/2} \cdot \mathbb{R} \cdot \mathbf{U} \cdot \mathbf{M}_N \cdot \mathbf{M}_{N-1} \cdots \mathbf{M}_1 \cdot \mathbf{S}_1 \cdot \mathbf{D}^{1/2} \tag{C.6}$$

*For these abbreviations, see the caption of TABLE 2.3 on p. 13.

†We do not present the figures of all the intermediate states. The first and the last figures of each transfer matrix correspond to (b) and (f) in FIGURE A.2 on p. 54, respectively. The middle one denotes a state right after the step-transfer matrix $\mathbf{M}_n$ has acted on.

with

$$\mathbf{M}_n(\bar{\tau}|\bar{\sigma}) = \left(\prod_{i \neq n} \delta_{\tau_i,\sigma_i} \right) , \tag{C.7}$$

$$\mathbf{U}(\tau|\bar{\sigma}) = \left(\prod_{i=1}^{N} \delta_{\tau_i,\sigma_i} \right) \{1 - \sigma_N \sigma_{N+1}\} . \tag{C.8}$$

TYPE (c). [lattice=triangle, direction=PD, interaction=(2+1), unit slice=(β), configuration space=$\psi_2^{(\beta)}$, non-symmetric] In this case, we apply the periodic conditions for each configuration, that is, $\tau_{n+N} = \tau_n$ for any n.

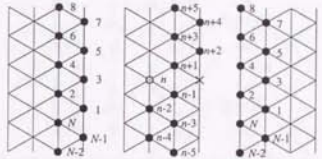

$$\mathbf{T} = \mathbf{D}^{1/2} \cdot \mathbf{M}_N \cdot \mathbf{M}_{N-2} \cdots \mathbf{M}_2 \cdot \mathbf{M}_{N-1} \cdot \mathbf{M}_{N-3} \cdots \mathbf{M}_1 \cdot \mathbf{D}^{1/2} \tag{C.9}$$

with

$$\mathbf{M}_n(\bar{\tau}|\bar{\sigma}) = \left(\prod_{i \neq n} \delta_{\tau_i,\sigma_i} \right) \exp[W_2 \tau_n \{\sigma_{n-3} + \sigma_n + \sigma_{n+3}\}] , \tag{C.10}$$

$$\mathbb{G}(\tau|\sigma) = \mathbb{R}(\tau|\sigma) , \tag{C.11}$$

and $\sigma_{N+k} = \sigma_k$ for any k.

TYPE (d). [lattice=triangle, direction=PL, interaction=(2+1), unit slice=(γ), configuration space=ϕ, non-symmetric] In this case, the definition is somewhat different from the others.

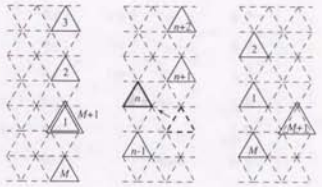

$$\mathbf{T} = \mathbf{D}^{1/2} \cdot \mathbf{U} \cdot \mathbf{M}_M \cdot \mathbf{M}_{M-1} \cdots \mathbf{M}_1 \cdot \mathbf{S}_1 \cdot \mathbf{D}^{1/2} \tag{C.12}$$

with

$$\mathbb{M}_m(\tilde{t}|\tilde{s}) = \left(\prod_{i\neq m}\delta_{t_i,s_i}\right) b_1(t_m|s_m)\, b_2(t_m|s_{m+1})\,, \tag{C.13}$$

$$\mathbb{U}(t|\tilde{s}) = \prod_{i=1}^{M}\delta_{t_i,s_i}\,, \tag{C.14}$$

where $M = N/3$, t_i and s_i $(= 0, 1, 2, 3)$ denote one of the possible states on a triangle (FIGURE B.1 (c)), and b_1 and b_2 are 4×4 matrices:

$$b_1(t|s) = \begin{pmatrix} 1 & 1 & 1 & 1 \\ 1 & e^{W_2} & 1 & 1 \\ 1 & 1 & e^{W_2} & 1 \\ 1 & 0 & 0 & e^{W_2} \end{pmatrix}, \tag{C.15}$$

$$b_2(t|s) = \begin{pmatrix} 1 & 1 & 1 & 1 \\ 1 & e^{W_2} & 0 & 1 \\ 1 & 1 & e^{W_2} & 1 \\ 1 & 1 & 0 & e^{W_2} \end{pmatrix}. \tag{C.16}$$

In practice, we use $\mathbb{T}' = \mathbb{R}\cdot\mathbb{T}^2$. For $\mathbb{T}'$, the conjugation matrix $\mathbb{G}$ can be defined as

$$\mathbb{G}(t|s) = \prod_{i=1}^{M} g(t_i|s_i) \tag{C.17}$$

with

$$g(t|s) = \begin{pmatrix} 1 & 0 & 0 & 0 \\ 0 & 1 & 0 & 0 \\ 0 & 0 & 0 & 1 \\ 0 & 0 & 1 & 0 \end{pmatrix}. \tag{C.18}$$

TYPE (e). [lattice=square, direction=RR, interaction=(2+1), unit slice=(α), configuration space=$\psi_2^{(o)}$, symmetric]

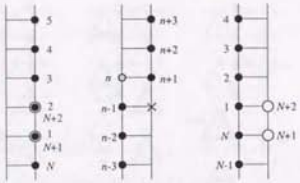

$$\mathbb{T} = \mathbb{D}^{1/2}\cdot\mathbb{R}\cdot\mathbb{U}\cdot\mathbb{M}_N\cdot\mathbb{M}_{N-1}\cdots\mathbb{M}_1\cdot\mathbb{S}_2\cdot\mathbb{D}^{1/2} \tag{C.19}$$

with

$$\mathbb{M}_n(\tilde{\tau}|\tilde{\sigma}) = \left(\prod_{i\neq n}\delta_{\tau_i,\sigma_i}\right)\exp[W_2\,\tau_n\,\{\sigma_n+\sigma_{n+2}\}]\,, \tag{C.20}$$

$$\mathbb{U}(\tau|\tilde{\sigma}) = \left(\prod_{i=1}^{N}\delta_{\tau_i,\sigma_i}\right)\{1-\sigma_N\sigma_{N+1}\}\,. \tag{C.21}$$

TYPE (f). [lattice=square, direction=DD, interaction=(2+1), unit slice=(δ), configuration space=$\psi_2^{(p)}$, non-symmetric]

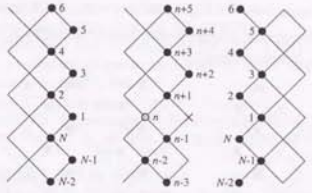

$$\mathbb{T} = \mathbb{D}^{1/2}\cdot\mathbb{M}_N\cdot\mathbb{M}_{N-2}\cdots\mathbb{M}_2\cdot\mathbb{M}_{N-1}\cdot\mathbb{M}_{N-3}\cdots\mathbb{M}_1\cdot\mathbb{D}^{1/2} \tag{C.22}$$

with

$$\mathbb{M}_n(\tau|\sigma) = \left(\prod_{i\neq n}\delta_{\tau_i,\sigma_i}\right)\exp[W_2\,\tau_n\,\sigma_n]\,, \tag{C.23}$$

$$\mathbb{G}(\tau|\sigma) = \mathbb{R}(\tau|\sigma)\,. \tag{C.24}$$

TYPE (g). [lattice=triangle, direction=PD, interaction=(3+0), unit slice=(β), configuration space=$\psi_3^{(o)}$, non-symmetric]

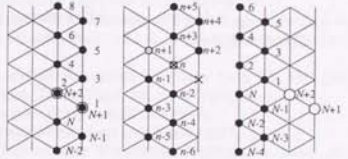

$$\mathbb{T} = \mathbb{D}^{1/2}\cdot\mathbb{R}^2\cdot\mathbb{U}\cdot(\mathbb{M}_{N-1}\cdot\mathbb{M}_{N-3}\cdots\mathbb{M}_1)^2\cdot\mathbb{S}_2\cdot\mathbb{D}^{1/2} \tag{C.25}$$

with

$$\mathbb{M}_n(\bar{\tau}|\bar{\sigma}) = \left(\prod_{i\neq n,n+1} \delta_{\tau_i,\sigma_i}\right) \delta_{\tau_n,\sigma_{n+1}} \times \{1-\tau_{n+1}\sigma_{n-2}\}\{1-\tau_{n+1}\sigma_{n+3}\}, \tag{C.26}$$

$$\mathbb{U}(\tau|\bar{\sigma}) = \left(\prod_{i=1}^{N} \delta_{\tau(i),\sigma(i)}\right) \{1-\sigma_{N-1}\sigma_{N+1}\} \times \{1-\sigma_{N-1}\sigma_{N+2}\}\{1-\sigma_N\sigma_{N+2}\}, \tag{C.27}$$

$$\mathbb{G}(\tau|\sigma) = \mathbb{R}(\tau|\sigma). \tag{C.28}$$

Here we assume $\sigma_{N+k+2} = \sigma_k$ for $k \geq 1$ and $\sigma_{-1} = \sigma_N$, for simple notations.

TYPE (h). [lattice=square, direction=DD, interaction=(3+0), unit slice=(δ), configuration space=$\psi_3^{(o)}$, non-symmetric]

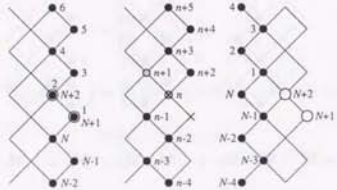

$$\mathbb{T} = \mathbb{D}^{1/2} \cdot \mathbb{R}^2 \cdot \mathbb{U} \cdot (\mathbb{M}_{N-1} \cdot \mathbb{M}_{N-3} \cdots \mathbb{M}_1)^2 \cdot \mathbb{S}_2 \cdot \mathbb{D}^{1/2}\} \tag{C.29}$$

with

$$\mathbb{M}_n(\bar{\tau}|\bar{\sigma}) = \left(\prod_{i\neq n,n+1} \delta_{\tau_i,\sigma_i}\right) \delta_{\tau_n,\sigma_{n+1}}, \tag{C.30}$$

$$\mathbb{U}(\tau|\bar{\sigma}) = \left(\prod_{i=1}^{N} \delta_{\tau_i,\sigma_i}\right) \{1-\sigma_{N-1}\sigma_{N+1}\} \times \{1-\sigma_{N-1}\sigma_{N+2}\}\{1-\sigma_N\sigma_{N+2}\}, \tag{C.31}$$

$$\mathbb{G}(\tau|\sigma) = \mathbb{R}(\tau|\sigma). \tag{C.32}$$

References

[1] L. D. Landau and E. M. Lifschitz, *Statistical Physics*, 3rd ed. (Pergamon, Oxford, 1980).
[2] L. K. Runnels, J. Chem. Ed. **47**, 742 (1970).
[3] R. Peierls, Proc. Camb. Phil. Soc. **32**, 471 (1936).
[4] Rushbrooke, Proc. Roy. Soc. (London) **A166**, 296 (1938).
[5] M. E. Fisher, in *Critical Phenomena*, edited by M. S. Green and J. V. Sengers (N.B.S., Washington, 1966), Vol. 273.
[6] C. N. Yang and T. D. Lee, Phys. Rev. **87**, 25 (1952).
[7] B. J. Alder and T. E. Wainwright, Phys. Rev. **127**, 359 (1962).
[8] E. Domany, M. Shick, J. S. Walker, and R. B. Griffiths, Phys. Rev. **B18**, 2209 (1978).
[9] M. Schick, Prg. Surf. Sci. **11**, 245 (1981).
[10] H. A. Kramers and G. H. Wannier, Phys. Rev. **60**, 252 (1941).
[11] H. A. Kramers and G. H. Wannier, Phys. Rev. **60**, 263 (1941).
[12] L. Onsager, Phys. Rev. **65**, 117 (1944).
[13] R. J. Baxter, *Exactly Solved Models in Statistical Mechanics* (Academic Press, London, 1982).
[14] M. P. Nightingale, in *Finite Size Scaling and Numerical Simulation of Statistical Systems*, edited by V. Privman (World Scientific, Singapore, 1990).
[15] A. A. Belavin, A. M. Polyakov, and A. B. Zamolodchikov, Nucl. Phys. **B241**, 333 (1984).
[16] J. L. Cardy, Nucl. Phys. **B270 [FS16]**, 186 (1986).
[17] C. J. Cardy, in *Phase Transitions and Critical Phenomena*, edited by C. Domb and J. L. Lebowitz (Academic Press, London, 1987), Vol. 11.
[18] P. Criste and M. Henkel, *Introduction to conformal invariance and its applications to critical phenomena* (Springer-Verlag, Berlin, 1993).
[19] M. E. Fisher, in *Critical Phenomena*, Proceedings of the 51st Enrico Fermi Summer School, Varenna, Italy, edited by M. S. Green (Academic Press, London, 1971).
[20] M. E. Fisher and M. N. Barber, Phys. Rev. Lett. **28**, 1516 (1972).
[21] M. Suzuki, Prog. Theor. Phys. **58**, 1142 (1977).
[22] M. P. Nightingale, Physica **A83**, 561 (1976).
[23] M. P. Nightingale, Phys. Lett. **A59**, 486 (1977).
[24] M. P. Nightingale, Proc. Koninklijke Nederlandse Acad. van Wetenschappen **B82**, 245 (1978).
[25] M. P. Nightingale, J. Appl. Phys. **53**, 7927 (1982).

[26] M. N. Barber, in *Phase Transitions and Critical Phenomena*, edited by C. Domb and J. L. Lebowitz (Academic Press, London, 1983), Vol. 8.
[27] V. Privman, in *Finite Size Scaling and Numerical Simulation of Statistical Systems*, edited by V. Privman (World Scientific, Singapore, 1990).
[28] C. Lanczos, J. Res. Nat. Bur. Standards **45**, 255 (1950).
[29] J. H. Wilkinson, *The Algebraic Eigenvalue Problem* (Oxford University Press, New York, 1965).
[30] J. Stoer and R. Bulirsch, *Introduction to Numerical Analysis*, 2nd ed. (Springer-Verlag, New York, 1992).
[31] H. W. J. Blöte, F. Y. Wu, and X. N. Wu, Int. J. Mod. Phys. **B4**, 619 (1990).
[32] V. Privman and M. E. Fisher, Phys. Rev. **B30**, 322 (1984).
[33] R. J. Baxter, J. Phys. A: Math. Gen. **13**, L61 (1980).
[34] D. S. Gaunt and M. E. Fisher, J. Chem. Phys. **43**, 2840 (1965).
[35] R. J. Baxter, I. G. Enting, and S. K. Tsang, J. Stat. Phys. **22**, 465 (1980).
[36] J. M. Ziman, Proc. Phys. Soc. **64A**, 1108 (1951).
[37] P. W. Kasteleijn, Physica **22**, 387 (1956).
[38] D. M. Burley, Proc. Phys. Soc. **75**, 452 (1960).
[39] A. Lipowski and M. Suzuki, J. Phys. Soc. Jpn. **61**, 2484 (1992).
[40] Z. Ràcz, Phys. Rev. **B21**, 4012 (1980).
[41] H. Meirovitch, J. Stat. Phys. **30**, 681 (1983).
[42] L. K. Runnels and L. L. Combs, J. Chem. Phys. **45**, 2482 (1966).
[43] A. Bellemans and R. K. Nigam, J. Chem. Phys. **46**, 2922 (1967).
[44] H. W. J. Blöte and X. N. Wu, J. Phys. A: Math. Gen. **23**, L627 (1990).
[45] G. Kamieniarz and H. W. Blöte, J. Phys. A: Math. Gen. **26**, 6679 (1993).
[46] E. Müller-Hartmann and J. Zittartz, Z. Phys. **B27**, 261 (1977).
[47] G. v. Gehlen, V. Rittenberg, and T. Vescan, J. Phys. **A20**, 2577 (1987).
[48] R. Bulirsch and J. Stoer, Numer. Math. **6**, 413 (1964).
[49] D. Shanks, J. Math. Phys. **34**, 1 (1955).
[50] D. Levin, Int. J. Comput. Math. **B3**, 371 (1973).
[51] J. M. van den Broeck and L. W. Schwartz, SIAM J. Math. Anal. **10**, 658 (1979).
[52] M. Henkel and G. Schütz, J. Phys. A: Math. Gen. **21**, 2617 (1988).
[53] D. C. Joyce, SIAM Rev. **13**, 435 (1971).
[54] D. A. Smith and W. F. Ford, SIAM J. Numer. Anal. **16**, 223 (1979).
[55] A. J. Guttmann, in *Phase Transitions and Critical Phenomena*, edited by C. Domb and L. J. Lebowitz (Academic Press, London, 1989), Vol. 13.
[56] E. J. Weniger, Comp. Phys. Rep. **10**, 189 (1989).
[57] C. J. Hamer, J. Phys. A: Math. Gen. **15**, L675 (1982).
[58] C. J. Hamer, J. Phys. A: Math. Gen. **16**, 3085 (1983).
[59] N. C. Bartelt, T. L. Einstein, and L. D. Roelofs, Phys. Rev. **B34**, 1616 (1986).
[60] J. Orban and A. Bellemans, J. Chem. Phys. **49**, 363 (1968).
[61] L. K. Runnels, J. R. Craig, and H. R. Streiffer, J. Chem. Phys. **54**, 1234 (1971).
[62] S. Todo and M. Suzuki, in *Hayashibara Forum '95 International Symposium on Coherent Approaches to Fluctuations* (World Scientific, Singapore, 1996).
[63] J. L. Cardy, J. Phys. A: Math. Gen. **19**, L1093 (1986).
[64] R. J. Baxter, J. Stat. Phys. **26**, 427 (1981).
[65] D. A. Huse, Phys. Rev. Lett. **49**, 1121 (1982).

[66] R. J. Baxter and P. A. Pearce, J. Phys. A: Math. Gen. **16**, 2239 (1983).
[67] W. Kinzel and M. Schick, Phys. Rev. **B24**, 324 (1981).
[68] G. F. Andrews, R. J. Baxter, and P. J. Forrester, J. Stat. Phys. **35**, 193 (1984).
[69] D. A. Huse, Phys. Rev. **B30**, 3908 (1984).
[70] P. Wills, J. Phys. A: Math. Gen. **20**, 5219 (1987).
[71] A. Yamagata, Physica **A215**, 511 (1995).
[72] A. Yamagata, Physica **A222**, 119 (1995).
[73] A. Yamagata, preprint (cond-mat/9510101).
[74] L. van Hove, Physica **15**, 951 (1949).
[75] F. Iglói, Phys. Rev. **B40**, 2362 (1989).
[76] L. Turban, J. Phys. C: Cond. Mat. **15**, L65 (1982).
[77] K. A. Penson, R. Jullien, and P. Pfeuty, Phys. Rev. **B26**, 6334 (1982).
[78] P. Pfeuty, Ann. Phys. (N.Y.) **57**, 79 (1970).
[79] H. W. Blöte, J. Phys. A: Math. Gen. **20**, L35 (1987).
[80] F. C. Alcaraz and M. N. Barber, J. Phys. A: Math. Gen. **20**, 179 (1987).
[81] C. Vanderzande and F. Iglói, J. Phys. A: Math. Gen. **20**, 4539 (1987).
[82] F. Iglói, J. Phys. A: Math. Gen. **20**, 5319 (1987).
[83] F. Iglói, D. Kapor, M. Škrinjar, and J. Sólyom, J. Phys. A: Math. Gen. **19**, 1189 (1986).
[84] F. C. Alcaraz, Phys. Rev. **B34**, 4885 (1986).
[85] K. A. Penson, J. M. Debierre, and L. Turban, Phys. Rev. **B37**, 7884 (1988).
[86] F. Mallezie, Phys. Rev. **B41**, 4475 (1990).
[87] M. P. M. den Nijs, J. Phys. A: Math. Gen. **12**, 1857 (1979).
[88] R. W. Zwanzig, J. Chem. Phys. **22**, 1420 (1954).
[89] J. A. Barker and D. Henderson, Rev. Mod. Phys. **48**, 587 (1976).
[90] D. Levesque, J. J. Weis, and J. P. Hansen, in *Applications of the Monte Carlo Method in Statistical Physics*, edited by K. Binder (Springer-Verlag, Berlin, 1984).
[91] K. J. Strandburg, Rev. Mod. Phys. **60**, 161 (1988).
[92] L. V. Woodcock, Ann. N.Y. Acad. Sci. **371**, 274 (1981).
[93] W. Vermöhlen and N. Ito, Int. J. Mod. Phys. **C5**, 1021 (1994).
[94] W. G. Hoover and F. H. Ree, J. Chem. Phys. **49**, 3609 (1968).
[95] J. Lee and K. J. Strandburg, Phys. Rev. **B46**, 11186 (1992).
[96] J. A. Zollweg and G. V. Chester, Phys. Rev. **B46**, 11190 (1992).
[97] M. Born and H. S. Green, Proc. Roy. Soc. (London) **A188**, 10 (1946).
[98] J. K. Percus and G. J. Yevick, Phys. Rev. **110**, 1 (1958).
[99] J. S. Rowlingson, Repts. Prog. Phys. **28**, 169 (1965).
[100] J. G. Kirkwood, J. Chem. Phys. **3**, 300 (1935).
[101] J. G. Kirkwood, J. Chem. Phys. **7**, 919 (1939).
[102] J. G. Kirkwood and E. M. Boggs, J. Chem. Phys. **10**, 394 (1942).
[103] E. Thiele, J. Chem. Phys. **39**, 474 (1963).
[104] M. S. Wertheim, Phys. Rev. Lett. **10**, 321 (1963).
[105] M. S. Wertheim, J. Math. Phys. **5**, 643 (1964).
[106] N. F. Carnahan and K. E. Starling, J. Chem. Phys. **51**, 635 (1969).
[107] M. J. Maeso, J. R. Solana, J. Amorós, and E. Villar, J. Chem. Phys. **94**, 551 (1991).

[108] X. Hu and M. Suzuki, J. Phys. Soc. Jpn. **62**, 2636 (1993).
[109] M. Suzuki, J. Phys. Soc. Jpn. **55**, 4205 (1986).
[110] M. Suzuki, M. Katori, and X. Hu, J. Phys. Soc. Jpn. **56**, 3092 (1987).
[111] M. Suzuki *et al.*, *Coherent anomaly method: mean field, fluctuations and systematics* (World Scientific, Singapore, 1995).
[112] S. Todo and M. Suzuki, J. Phys. Soc. Jpn. **63**, 3552 (1994).
[113] N. J. A. Sloane, Scientific American Jan. 92 (1984).
[114] L. Tonks, Phys. Rev. **50**, 955 (1936).
[115] L. Boltzmann, Verslag Gewone Vergadering Afdeling Natuurkunde Koninklike Nederlandse Akademie Wetenschap **7**, 484 (1899).
[116] H. Happel, Ann. Physik **21**, 342 (1906).
[117] J. J. van Laar, Amsterdam Akad. Verslag **7**, 350 (1899).
[118] B. R. A. Nijboer and L. van Hove, Phys. Rev. **85**, 777 (1952).
[119] J. S. Rowlinson, Mol. Phys. **7**, 593 (1964).
[120] P. C. Hemmer, J. Chem. Phys. **42**, 1116 (1965).
[121] F. H. Ree and W. G. Hoover, J. Chem. Phys. **40**, 939 (1964).
[122] F. H. Ree and W. G. Hoover, J. Chem. Phys. **46**, 4181 (1967).
[123] J. S. Rowlinson, Proc. Roy. Soc. (London) **A279**, 147 (1964).
[124] S. Kim and D. Henderson, Phys. Lett. **27A**, 378 (1968).
[125] J. E. Kilpatrick, Advan. Chem. Phys. **20**, 39 (1971).
[126] K. W. Kratky, Physica **A85**, 607 (1976).
[127] K. W. Kratky, Physica **A87**, 584 (1977).
[128] K. W. Kratky, J. Stat. Phys. **27**, 533 (1982).
[129] K. W. Kratky, J. Stat. Phys. **29**, 129 (1982).
[130] E. J. Janse van Rensburg and G. M. Torrie, J. Phys. A: Math. Gen. **26**, 943 (1992).
[131] E. J. Janse van Rensburg, J. Phys. A: Math. Gen. **26**, 4805 (1993).
[132] M. Luban and A. Baram, J. Chem. Phys. **76**, 3233 (1982).
[133] W. Vermöhlen and N. Ito, Phys. Rev. **E51**, 4325 (1995).
[134] M. P. M. den Nijs, M. P. Nightingale, and M. Schick, Phys. Rev. **B26**, 2490 (1982).
[135] M. T. Batchelor, J. Aust. Math. Soc. **B26**, 462 (1987).
[136] L. K. Runnels, L. L. Combs, and J. P. Salvant, J. Chem. Phys. **47**, 4015 (1967).